Energy Conversion and Management 345 (2025) 120394

Contents lists available at ScienceDirect

Energy Conversion and Management

journal homepage: www.elsevier.com/locate/enconman

Research Paper

On the influence of the H_2 flame thermo-diffusive instability at engine-like conditions: A CFD-driven study

Stefano Sfriso [a,*], Fabio Berni [a], Sebastiano Breda [a], Caio Ramalho Leite [b], Fabriche Foucher [b], Pierre Bréquigny [b], Jacques Borée [c], Stefano Fontanesi [a]

[a] Università di Modena e Reggio Emilia, Italy
[b] University of Orléans, France
[c] ISAE-ENSMA, France

ARTICLE INFO

Keywords:
3D-CFD
H2 combustion
Thermo-diffusive instability
Turbulence-instability interaction
ICE

ABSTRACT

The effect of thermo-diffusive (TD) instabilities on combustion of lean and ultra-lean mixtures is one of the most debated aspects in the field of hydrogen internal combustion engines (ICEs). This paper presents a numerical setup for 3D-CFD in-cylinder simulations of H2 ICEs and, by adopting it, the effect of the TD instability is assessed.

An initial setup relying on G-equation to represent the flame propagation is presented, with a Damköhler-like correlation for the turbulent flame speed and Verhelst polynomial correlation for the laminar one. Then the simulation setup is improved by three key modifications. In order, a correction factor to account for TD instability, the turbulence-instability interaction and a wall quenching model are progressively added to obtain the final setup. The results at each stage of the framework development are compared with experiments at six operating points, and the discrepancies are analyzed. All the operating points are characterized by lean/ultra-lean mixtures, with equivalence ratios ranging from 0.30 to 0.55. The investigated powertrain is a port-fuel injection (PFI) spark-ignition hydrogen research ICE. Port-fuel injection and resulting homogeneous mixture eliminate the uncertainties related to the stratification and allow the research activity to be completely focused on combustion dynamics.

Firstly, the findings highlight that the effect of the TD instability is a slight modification of in-cylinder pressure and combustion indicators at the examined engine conditions. Secondly, the addition of both turbulence-instability interaction and wall quenching of the flame has a similar (and opposite) effect compared to the TD instability one. Therefore, comparing the results provided by the initial and final numerical frameworks, they are similar and both close to the experiments. Despite the fortuitous compensation at the presently investigated conditions, in order to perform accurate simulations, it is necessary to account for both TD instability and wall quenching phenomena. This is even more true considering that, at different conditions, the instability effect may differ and be much more significant.

1. Introduction

The increasing concern about climate change due to greenhouse gas emissions has recently pushed the EU to tighten the CO_2 emissions performance standards for on-road transportation [1]. In particular, starting from 2035, new passenger cars and light commercial vehicles have to emit zero carbon dioxide. This bans, de facto, ICEs fuelled by traditional fossil fuels. However, ICEs running on green hydrogen (H_2) or carbon–neutral fuels could still be adopted. The former does not produce CO_2 at the exhaust. The latter, like e-gasoline or biofuels (e.g. biodiesel), are characterized by CO_2 emissions which are compensated by the amount absorbed during their production [2]. As for the carbon-based e-fuels, the CO adopted in the industrial process to obtain the final product comes from CO_2 captured from the atmosphere, while biofuels are derived from biomass absorbing CO_2 during formation. As a result, although ICEs powered by carbon-based e-fuels or biofuels cannot be classified as zero tailpipe-emission solutions, they are carbon neutral anyway. Not surprisingly, the EU regulation [1] leaves the door open for

* Corresponding author.
E-mail address: stefano.sfriso@unimore.it (S. Sfriso).

https://doi.org/10.1016/j.enconman.2025.120394
Received 4 June 2025; Received in revised form 28 July 2025; Accepted 15 August 2025
Available online 25 August 2025

the use of carbon-based e-fuels or biofuels in ICEs after 2035.

Focusing on green H_2, it is a renewable e-fuel produced via electrolysis, using H_2O and electric energy coming from renewable sources (such as wind).

In ICEs, H_2 can significantly contribute to pollutant emissions reduction. Only nitrogen oxides (NO_x) [3] can be found as a pollutant in the exhaust gasses. However, traces of unburnt hydrocarbons, soot and CO_2 can be found at the tailpipe, because of the reactions involving the lubricating oil in the cylinder [4]. This is the main reason why, currently, H_2 ICEs are formally not accepted yet by the EU for the survival of the internal combustion engine after 2035.

From a purely technological perspective, hydrogen could play a crucial role in keeping a well-consolidated, valid and robust technology such as the ICE. Even if battery electric or fuel cell vehicles are considered zero emission solutions by the EU, they suffer from problems related, for instance, to sustainability and degradation.

In terms of scientific research, H_2 ICEs are not a novelty. Several publications on the topic can be found in the literature, dealing with both experiments and numerical simulations. The review proposed in the following deals with numerical works, with a specific focus on the TD instability. In particular, some recent works are reviewed and categorized into those neglecting the TD flame instability and those that consider it.

Starting from the first category, the works are based on different combustion models, such as detailed chemistry and flamelet ones. Millo et al. [5] propose a synergic 0D/1D/3D approach for H_2 internal combustion engines, where combustion is simulated via a 3D approach based on detail chemistry (SAGE model) with Zhang's [6] mechanism. Liu et al. [7] and Babayev et al. [8] utilize the SAGE model for hydrogen combustion in turbulent jet ignition (TJI) and compression ignition engines, respectively. Other publications rely on flamelet models, such as the Coherent Flame Model (CFM) or its "Extended" version (ECFM). For instance, Pielecha et al. [9] use CFM in a numerical study of a TJI hydrogen engine, though no validation is provided. Rouleau et al. [10] adopt ECFM to investigate a high-compression-ratio direct-injection (DI) hydrogen engine. Maio et al. [11] compare 3D-CFD results obtained by ECFM with experimental data on a hydrogen engine equipped with both PFI and DI. Knop et al. [12] study two hydrogen engines, one PFI with a cryogenic injection system and one DI, using ECFM. Finally, Piano et al. [13] utilize ECFM-3Z to investigate abnormal combustion on a single operating condition with two different coolant temperatures. However, the CFM- and ECFM-based studies presented above show scarce validation against experiments. In fact, only a limited number of operating conditions is tested. Additionally, in some works, a case-to-case calibration of the combustion model is required, highlighting the limited predictive capabilities of the proposed numerical frameworks. Other research groups combine the flamelet model with complex chemistry. For instance, Berni et al. [14] employ the G-equation along with detailed chemistry for real-time calculation of the burnt gas composition. In this case, the heat release rate is determined by the combined effect of the G-equation and detailed chemistry. The study proposes a numerical analysis of performance, heat transfer, knock and emissions on an ICE fuelled with NH_3-H_2 mixtures (including pure H_2 and pure NH_3).

Among the papers that integrate the effect of TD flame instability in their numerical framework, level-set techniques are mostly adopted. Kosmadakis et al. [15] propose a formulation which considers the flame instability by using a laminar flame speed (LFS) correlation derived from experimental measurements including instability effects [16]. Ramognino et al. [17] introduce the flame instability effect through an empirical power law correlation proposed by Berger [18] and derived from direct numerical simulations (DNS) of 2D flames. The correlation corrects the unstretched LFS values provided by a look-up table generated by 1D chemical kinetic computations. Hernandez et al. [19] simulate ultra-lean combustion using G-equation combined with tabulated chemistry to calculate the laminar flame speed. In order to consider the instability effect, LFS is corrected through an empirical correlation proposed by Howarth [20]. Such a correlation is based on the TD contribution to the flame instability growth rate, and it is obtained thanks to 3D DNS flame simulations. A similar approach is used by Novella et al. [21], who adopt G-equation with Peters' correlation for the turbulent flame speed and a tabulated LFS. As for this last quantity, the values present in the table are already corrected through the Howarth correlation.

Interestingly, the works reviewed above rely on different ways to account for the H_2 flame TD instability, with the last two employing the method which is the most promising one. In fact, in the first work, the instability effect is inherently included in the adopted LFS. Therefore, it is impossible to separate the unstretched LFS from the corrected one. However, this separation is essential to include the turbulence-instability interaction in the modeling framework. As for the DNS-based approaches, the one based on the 3D flame simulation outcomes is preferable. In [20,22], it is demonstrated that the impact of the TD instability on LFS differs between 2D and 3D simulations and, obviously, a 3D approach can be considered more accurate for the evaluation of the impact.

In conclusion, the most recent literature features both works that account for TD instability and those that neglect it. Among the papers including the effect, none of them simultaneously addresses ultra-lean conditions and presents validation on several operating points with a unique set of calibration parameters (i.e. without dedicated tuning for each single case). In addition, none of the papers accounts for turbulence-instability interaction. In fact, Hernandez et al. [19] and Ramognino et al. [17] propose unstretched laminar flame speed correction only, while Novella et al. [21] introduce additionally a modeling of flame quenching based on the Peclet number, but still no attempt to consider the turbulence-instability interaction is made.

The present paper aims to fill these gaps, by introducing and validating a 3D-CFD numerical setup for in-cylinder simulations of H_2 ICEs at multiple operating conditions. The framework considers the impact of the TD instability, by correcting the unstretched LFS with the empirical correlation suggested by Howarth. As described above, this is the most promising method to model the instability effects in combustion simulations. In addition, the setup accounts for the interaction between turbulence and instability, which is the main novelty of the present work, compared to the existing literature. Lastly, a wall quenching model is implemented in the numerical framework. The 3D numerical setup is validated against a set of experimental data on ultra-lean operating conditions, by using a single set of calibration parameters. The setup exploits the G-equation combustion model where the LFS is computed through the Verhelst's [23] correlation and a Damköhler-derived formulation for the turbulent flame speed [24,25,26] is adopted. The experiments are performed on an optical engine derived from the gasoline PSA EP6 engine.

It should be noted that the framework presented here was already employed and validated in [27,28] by the authors, but in a simpler form (i.e. without flame instability, turbulence-instability interaction and quenching) hereafter referred to as 'base' setup. Both in [27,28], the 'base' framework was tested on a DI H_2 engine derived from a Diesel unit, on 11 operating points characterized by equivalence ratios (φ) and revving speeds spanning from 0.4 to 0.8 and from 1500 to 3000 rpm, respectively. In [29], the 'base' setup was adopted to analyze the PSA EP6 engine investigated in the present work. Even in that case, the results strongly agreed with the experiments. Interestingly, the calibration parameters of the combustion and ignition models were the same for the two engines. The agreement with the experiments obtained on two different engines and without the effect of TD instability raised the question, in the authors, on its actual impact at engine-like conditions.

For this reason, in the present work, the 3D numerical setup is further refined by including instability, along with its interaction with turbulence and wall quenching. The advanced setup (hereafter referred to as 'improved') is tested on the H_2 PSA EP6 engine, as it is characterized by homogeneous mixture which eliminates any numerical uncertainty

related to the stratification.

After the introduction, investigated ICE and experimental test bench are presented. Then, the numerical setup is described, with focus on the modeling approach for the TD instability effect. The result section of this paper starts with the outcomes of the previous work [29], obtained with the simplified setup (i.e. without flame instability and quenching). Then, effects of TD instability, turbulence-instability interaction and flame quenching are progressively included and, finally, the need to consider the TD instability effect is discussed.

2. Investigated engine and experimental apparatus

This paper investigates a four-valve spark-ignition (SI) optical engine, whose key geometric specifications are provided in Table 1. Fig. 1 displays the engine installed at the test bench, where long intake and exhaust pipes and large plenums are visible. The increased pipe length is designed to allow for enhanced mixing of fuel and air before entering the combustion chamber and to provide more robust boundary conditions away from the intake and exhaust valves. The engine is equipped with a Bosch ZLR07MTE spark plug, purposely selected for hydrogen applications and characterized by three mass electrodes. It offers a balance between minimizing cycle-to-cycle variability at low loads and extending the knock limit at high loads.

In order to obtain a homogeneous air–fuel mixture, H_2 is continuously injected near the intake plenum, to maximize the distance from the intake valves. Fig. 2 illustrates the test bench layout. As it can be seen, the instantaneous pressure is measured in the cylinder and plenums. These quantities are obtained using a quartz pressure piezoelectric transducer (AVL QH32C) in the cylinder, characterized by a pressure range up to 200 bar, a sensitivity of 26.82 pC/bar, and a linearity error equal to ±0.25 % of full scale. The temperatures in the intake and exhaust pipes are measured as well, while the desired mixture quality is obtained by means of Coriolis mass flowmeters of air and hydrogen, installed upstream of the intake plenum. Further details on the experimental apparatus can be found in [30].

The operating conditions analyzed in the present work are summarized in Table 2. The cases share the same spark timing, intake pressure and engine speed, but φ spans from 0.30 to 0.55.

3. 3D-CFD numerical setup

3.1. Boundary conditions

A fully homogeneous mixture at a given equivalence ratio (based on the operating condition) is enforced at the inlet boundary, consistently with the experiments that maximize the mixture uniformity thanks to the H_2 injection occurring close to the plenum (i.e. far from the intake valve). At both the intake and exhaust boundaries, time-varying pressure conditions are applied during the simulation, obtained by averaging 100 experimentally measured instantaneous traces. As for the temperature, due to the limitations of the thermocouples (not fast enough to track rapid fluctuations), only cycle-averaged data are available and they are imposed at the boundaries. Uniform (but component-dependent) wall temperatures are set following the authors' experience [32,33,34]. The values adopted in this work can be found in [31].

Table 1
Engine geometrical characteristics.

Bore	77 mm
Stroke	85.8 mm
Displacement	400 cm^3
Compression ratio	10.5:1
Connecting rod length	138.5 mm
Pin offset	0.8 mm
No. of valves	4

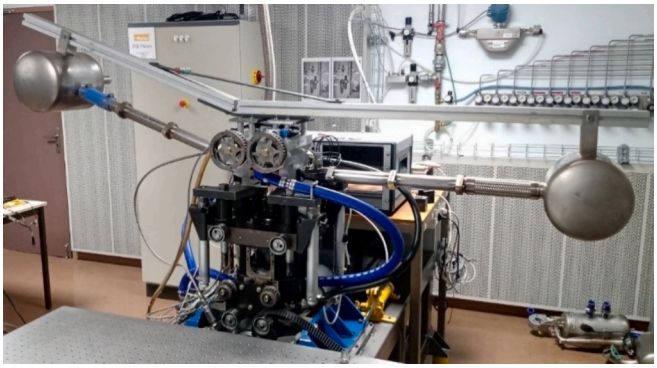

Fig. 1. Single-cylinder engine with intake/exhaust ducts and plenums [30].

3.2. Numerical setup

Based on the authors' experience with the software, STAR-CD, licensed by SIEMENS DISW, is adopted to perform the in-cylinder simulations. An unsteady Reynolds-averaged Navier-Stokes (URANS) approach is employed, with the k-ε RNG [35,36] to model turbulence, which has been extensively adopted in both literature and previous works by the authors [37,38,39,40,41,42].

For the near-wall flow modeling, a single prismatic layer of 0.3 mm thickness is applied at the walls, along with a high-Reynolds approach to minimize the computational effort. The Improved GruMo-UniMORE [43,44,45] is chosen to model the wall heat transfer.

The time-step is 0.05° CA during ignition, combustion and valve motion, while in the remaining parts of the cycle is 0.1° CA. Start and end of the simulations are fixed to 90° CA after top dead center (aTDC) and 810° CA aTDC, respectively, i.e. in the middle of the expansion stroke. For each investigated point, three consecutive cycles are run to minimize the effect of the initial conditions.

3.2.1. Ignition

Ignition is managed using an in-house developed sub-grid model that was extensively validated in a Large eddy simulations (LES) framework [46,47]. The model relies on initial estimates for flame kernel radius r_k and temperature T_k. These values serve as initial conditions for a 1D ordinary differential equation (ODE), which is solved from the spark-time until a threshold value for the kernel radius is reached. Interestingly, in this version of the model, it is assumed that the spark-time (from electronic control unit) coincides with the actual spark discharge, i.e. the delay of the electric circuit is considered negligible. The 1D ODE, similar to the Herweg and Maly formulation [48], is given in Eq. (1).

$$\frac{dr_k}{dt} = \frac{\rho_u}{\rho_k}(S_L + S_{Plasma}) + \frac{V_k}{A_k}\left[\frac{1}{T_k}\frac{dT_k}{dt}\right] \tag{1}$$

r_k is the kernel radius while ρ_u is the unburnt gas density. ρ_k, T_k, A_k and V_k are mean density and temperature, surface area and volume of the flame kernel. S_L is the unstretched LFS while S_{Plasma} is the plasma channel expansion velocity. Unlike [49], this approach does not include a transition from laminar to turbulent flame speed, i.e. only the first is considered.

As for the kernel radius threshold, a value of 2.3 mm is set, beyond which the solver stops computing r_k from Eq. (1). In fact, according to [48], the contribution of turbulence becomes significant for (roughly) $r_k > 2$ mm. Beyond this point, the flame propagation is controlled by the G-equation, relying on the prescribed turbulent flame speed.

S_{Plasma} is calculated by Eq. (2), namely the unsteady 1D equation for heat conduction. The calculation of S_{Plasma} assumes a spherical kernel, similarly to [49].

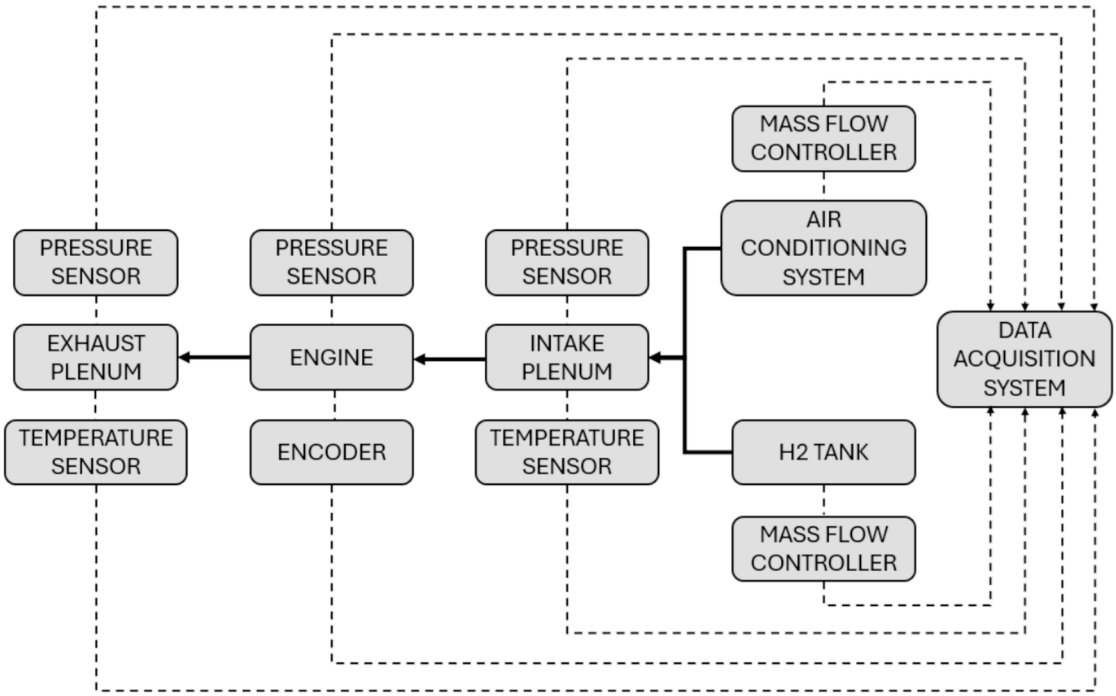

Fig. 2. Test bench layout [31].

Table 2
Analyzed operating conditions.

Case number	φ	Ignition [° CA BTDC]	Intake temperature [K]	Exhaust temperature [K]	Average intake pressure [bar]	rpm	CoV IMEP [%]
1	0.30	−15	295.7	596.0	0.70	1500	4.875
2	0.35	−15	295.7	608.6	0.70	1500	2.144
3	0.40	−15	295.8	623.7	0.70	1500	1.370
4	0.45	−15	295.9	635.0	0.70	1500	0.966
5	0.50	−15	296.0	658.4	0.70	1500	1.174
6	0.55	−15	296.0	666.2	0.70	1500	1.508

$$\rho c_p \frac{\partial T}{\partial t} = \frac{\partial}{\partial x}\left(k \frac{\partial T}{\partial x}\right) \tag{2}$$

In Eq. (2), apart from t and x that are time and radial coordinate, all the variables refer to plasma. ρ and c_p are density and specific heat, while T is the temperature and k is the thermal conductivity. The product ρc_p is held constant to 8000 J/(m^{3}K), while k is fixed at 0.2 W/(mK) [50–55]. As for the boundary conditions of Eq. (2), at $x = 0$, T is fixed to $60 \bullet 10^3$ K [48], corresponding to the plasma temperature. For $x \to \infty$, an adiabatic condition is imposed. As for the initial condition, T is fixed to the unburnt temperature of the mixture. S_{Plasma} is calculated as the temperature diffusion velocity (along x) from the plasma channel.

Eq. (1) initial condition (namely r_k initial value) is determined using a method similar to the one proposed by Colin and Benkenida [56]. The initial burnt mass volume ($V_{k,init}$) is calculated considering a cylinder with radius and height equal to flame thickness (δ_L) and spark gap (d_{gap}, equal to 0.5 mm), respectively. The initial spherical flame kernel radius is then derived by Eq. (4), which calculates the radius of a sphere whose volume is $V_{k,init}$.

$$V_{k,init} = d_{gap} \pi {\delta_L}^2 \tag{3}$$

$$r_{k,init} = \left(\frac{3}{4\pi} V_{k,init}\right)^{1/3} \tag{4}$$

δ_L values to be used in Eq. (3) are reported in Table 3 and they are determined through 1D steady-state flame simulations, performed with DARS v2020.1 licensed by SIEMENS DISW. The governing equations for the freely propagating flame model are detailed in the DARS user guide [57]. These simulations employ the kinetics mechanism developed by Konnov [58], and they are carried out at the spark-time conditions that are listed in Table 3.

Table 3
Pressure, temperature and equivalence ratio are reported for each case, computed as mass-weighted averages over the combustion chamber at the spark-time (705° CA). The calculated flame thickness and initial kernel radius values are reported as well.

Case number	p [bar]	T [K]	φ [–]	δ_l [mm]	r_k [mm]
1	11.4	732	0.30	0.168	0.220
2	11.4	732	0.35	0.096	0.151
3	11.4	732	0.40	0.068	0.120
4	11.4	732	0.45	0.056	0.106
5	11.4	732	0.50	0.050	0.098
6	11.4	732	0.55	0.049	0.097

The initial flame kernel radii calculated via Eqs. (3) and (4) are reported in the last column of Table 3. The laminar flame thickness is defined here as the distance between 5 % and 95 % of the maximum temperature reached in the simulation domain. As noticed, the resulting values are close and, on average, equal to $\sim 1 \bullet 10^{-4}$ m. This value is used as initial condition in Eq. (1). A sensitivity analysis (here omitted for brevity) shows that small changes in the initial value of r_k (i.e. within its order of magnitude) have a minimal impact in the results, as the rapid

kernel growth compensates for any minor variation.

3.2.2. Combustion

In the present paper, turbulent premixed combustion is modeled by G-equation. It employs a level-set method to track the scalar G, which represents the distance from the flame front (determined by the G = 0 *iso*-surface). A positive G value indicates burnt region, while a negative one identifies unburnt gasses. Eq. (5) represents the scalar G transport equation. More details are available in [27,59].

$$\frac{\partial}{\partial t}\rho G+\frac{\partial}{\partial x_i}\rho u_i G=\rho S_T|\nabla G| \tag{5}$$

The turbulent flame speed S_T is calculated using the Damköhler correlation, shown in Eq. (6).

$$S_T=S_L\left(1+A\bullet\left(\frac{u'}{S_L}\right)^{\frac{5}{6}}\right) \tag{6}$$

S_L is LFS and u' is the turbulent intensity defined as $u'=\sqrt{\frac{2}{3}tke}$, with *tke* representing the turbulent kinetic energy. The coefficient A is empirical and set to 3.3 in this study. LFS is calculated using Verhelst polynomial [23], fitting the results of chemical kinetics simulations based on Konnov mechanism [58]. This correlation does not account for flame acceleration due to TD instability, as it is derived from 1D steady-state freely propagating flame computations. Verhelst polynomial is interpolated in the following ranges of pressure (p), temperature (T), equivalence ratio (φ), and EGR: 5 bar ≤ p ≤ 45 bar, 500 K ≤ T ≤ 900 K, 0.33 ≤ φ ≤ 5, and 0 % ≤ EGR ≤ 50 %.

Interestingly, the only calibration parameters exploited in this work are the r_k threshold value present in the ignition model and the constant A in Eq. (6) (i.e. in the turbulent combustion model). Once calibrated, the same values are adopted in all the simulations presented in this paper, without any case-by-case variation, and they roughly correspond to the ones adopted in previous works by the authors [27,60], where neither TD instability nor flame quenching were considered. The only difference with respect to the past is the adoption of a r_k threshold of 2.3 mm instead of 2 mm. Such a slight variation is introduced to optimize the agreement with the experiments. The variation is anyway minimal, and the selected value remains coherent with those available in literature.

3.2.3. Flame thermo-diffusive instability

As discussed in the introduction, among the approaches able to model the TD instability effect on the flame propagation, the one proposed by Howarth [20] is preferred and adopted in the present work. The theoretical background of this approach is briefly resumed in the following.

As a first approximation, a flame can be assumed as an infinitely thin surface dividing two regions of gasses at different density. If an arbitrary disturbance characterized by sinusoidal wave form is applied to the flame and studied, it turns out that its growth rate is always positive, meaning that the flame is always unstable. In literature, this is referred to as "Darrieus-Landau (hydrodynamic) instability". In this case, the instability wave growth rate (ω) is given by the first term on the right side of Eq. (7). By refining the approach, the flame can be considered as a volume of finite thickness, where mass and thermal diffusivity phenomena should be considered. From a mathematical standpoint, this reflects in the presence of a second order term in the wave growth rate expression (second right hand side term in Eq. (7)). It can be positive, further destabilizing the flame and leading to faster and stronger instability, or negative, contributing to flame stabilization. The effective mixture Lewis number discerns the two conditions. With $Le_{eff}<1$, the flame is thermo-diffusively unstable. On the contrary, with $Le_{eff}>1$, the flame is thermo-diffusively stable. Interestingly, if $Le_{eff}>1$, the flame can still be stable or unstable. In fact, the resulting ω can be positive or negative, based on the magnitudes of the hydrodynamic and TD instability contributions.

Resuming, Eq. (7) reports the instability wave growth rate as described in [61], where both Darrieus-Landau and TD instabilities are considered.

$$\omega=\omega_{DL}S_L\varkappa-\delta_l\left[B_1+\beta\left(Le_{eff}-1\right)B_2+PrB_3\right]S_L\varkappa^2 \tag{7}$$

ω_{DL} is its first-order term. $\varkappa$ denotes the instability spectral component wave number, while δ_l is the laminar flame thickness and β is the Zel'-dovich number. Le_{eff} is the effective Lewis number of the mixture, calculated as in [61], and Pr is the Prandtl number of the mixture. Coefficients B_1, B_2, and B_3 are determined following the method described in the same Ref. [61]. In the following, the opposite of the expression inside the square brackets (namely $-\left[B_1+\beta\left(Le_{eff}-1\right)B_2+PrB_3\right]$) will be referred to as ω_2.

Since H_2 can burn at extremely lean equivalence ratios, it is possible to have very low effective mixture Lewis numbers, making lean hydrogen flames prone to the TD instability. Based on these considerations, Howarth [20] identifies ω_2 as a suitable candidate to relate the unstretched LFS (provided by experiments or 1D chemical kinetics simulations) to the one featuring TD instability and measured by 3D DNS simulations. The relationship between the two is resumed by Eq. (8).

$$\frac{S_{L\,instab}}{S_L}=\begin{cases}e^{0.08\bullet\omega_2} & if\ \ \varphi\geq\varphi_{lim}\\ 1+0.47\bullet\omega_2 & if\ \ \varphi<\varphi_{lim}\end{cases} \tag{8}$$

$\varphi_{lim}=(0.3475-0.000325\bullet T)\bullet p^{0.1425+0.000225\bullet T}$ is the equivalence ratio threshold that defines, for given pressure and temperature, the switch between the two correlations of Eq. (8). φ_{lim} expression represents the location of the peak values in ω_2 maps, created in a $p-\varphi$ plane for a fixed temperature. In other words, the φ_{lim} correlation divides a given ω_2 map in two regions where the correlations reported in Eq. (8) are valid (one per each region), as described in [20]. In this regard, Fig. 3 reports 3 maps in the $p-\varphi$ plane computed at 500, 700 and 900 K. An analysis of the maps reveals a clear dependency of ω_2 on temperature. Moving from one map to another characterized by higher temperature, all the points are characterized by lower ω_2 values. The effects of equivalence ratio and pressure do not follow this uniform trend, as the maps exhibit a crest. Overall, regardless of the map, starting from the upper left corner, increasing p and decreasing φ tends to destabilize the flame (i.e. higher ω_2 values are encountered). This occurs up to the crest. Then, moving on in the same direction, ω_2 values decrease, leading to flame stabilization.

3.2.4. Turbulence-instability interaction in the flame

Considering the TD instability effect via a correction of LFS may not be enough to comprehensively model the H_2 flame propagation. For instance, Matalon et al. [62,63] observed that, while increasing the turbulence intensity, the turbulent wrinkling tends to dominate the flame instabilities. More recently, Berger et al. [64] noted the dampening effect of the turbulence on the TD instability in DNS simulations of a slot burner. Therefore, proper combustion modeling cannot prescind the turbulence-instability interaction. In [65,66], Bradley introduced a method to quantify the relative contributions of turbulence and instability to the flame wrinkling, defining a parameter known as Karlovitz stretch factor. As per Bradley's formulation, Eq. (9) represents this factor.

$$K=0.25\cdot\left(\frac{u'}{S_L}\right)^2\cdot R_l^{-0.5} \tag{9}$$

The terms that appear in the equation are turbulent intensity u', laminar flame speed S_L and turbulent Reynolds number $R_l=\frac{u'l_t}{\nu}$, where l_t is the integral length scale and ν the kinematic viscosity.

In [65,66], Bradley et al. identified the "regime of laminar instabilities and mild turbulence" for $K\leq 0.1$ and the "fully turbulent

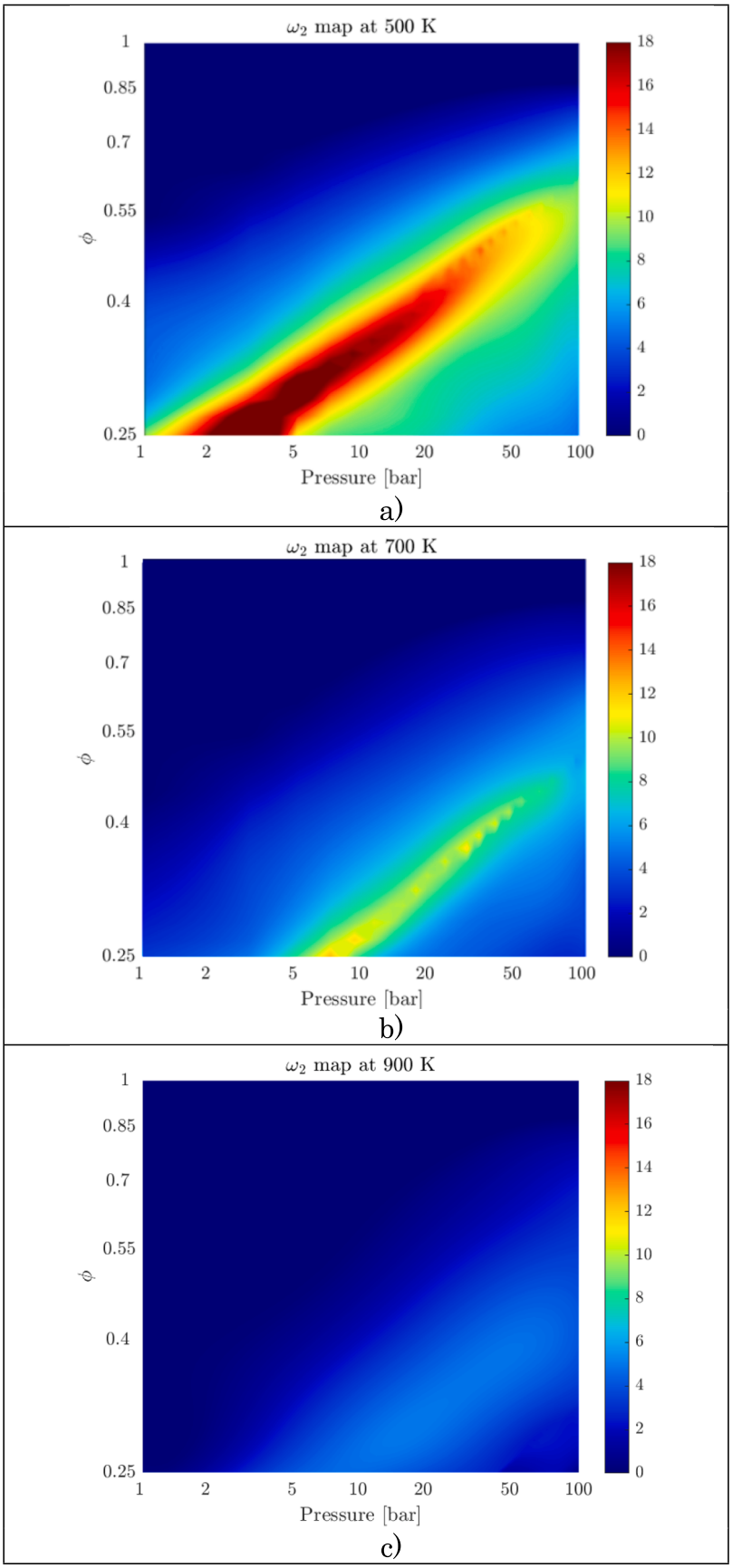

Fig. 3. ω_2 map at three different temperatures.

regime" for $K > 0.1$. In the former, the instability effect is significant. Conversely, in the latter, the turbulence wavelengths dominate and intensify the flame wrinkling, thus making the TD instability-induced wrinkling negligible.

In order to obtain a smooth transition between the two regimes, an S-shaped function is introduced and reported in Eq. (10). It guarantees continuity in the transition from S_L to $S_{L\,instab}$.

$$S_{L\,corrected} = S_L + \frac{1}{e^{100(K-0.1)} + \frac{1}{S_{L\,instab} - S_L}} \tag{10}$$

Fig. 4 reports an example of blending, with this function, between two arbitrary laminar flame speeds of 4 and 6 m/s.

The parameter 100, which appears in Eq. (10), is used as a calibration constant and governs the width of the 'S'. A much higher value leads to a step function. The other parameter, 0.1, is the threshold value for the Karlovitz stretch factor, acting as a center for the 'S'.

It is important to note that, with this approach to turbulence-chemistry interaction, the effects of instability and turbulence on the flame are de facto decoupled. In fact, by using the Karlovitz stretch factor, the instability effect is either completely inhibited or it is applied along with the turbulent one by the superimposition method (i.e. they are applied sequentially, at first LFS is corrected and, then, it is adopted to compute the turbulent one). While this assumption is not inherently incorrect, it requires validation. In other words, the superimposition method can be applied or not (i.e. a more complex approach is necessary), based on the characteristic scales of turbulence and instability. However, estimating the instability scales, which are essential for comparison with the turbulent ones, is a complex task and will be explored in future work.

3.2.5. Wall quenching

A simplified method is adopted to model the wall flame quenching. It relies on Eq. (11) [59], which calculates the quenching distance l_q. For any cell centroid, if the wall distance is smaller than l_q, LFS is adopted instead of the turbulent one.

$$l_q = f_q \left[11.5\mu / \left(\rho C_\mu^{0.25} tke^{0.5} \right) \right] \tag{11}$$

In Eq. (11), f_q is set to 1, following [59]. The other variables are density ρ, molecular viscosity μ, turbulent kinetic energy tke, and turbulent viscosity constant C_μ. The value 11.5 corresponds to the dimensionless wall distance (y^+) value defining the (ideal) transition between the viscous sub-layer and the log-region within the boundary layer. In practice, the model assumes that, when y^+ is lower than 11.5 (i.e. the cell centroid pertains to the viscous sub-layer), the impact of the turbulence-induced flame stretch is negligible. This is a simplification of the Bruneaux model [67], which applies a correction to the integral length scale for $y^+ < 50$, recognizing that vortices larger than their wall distance are unlikely to persist.

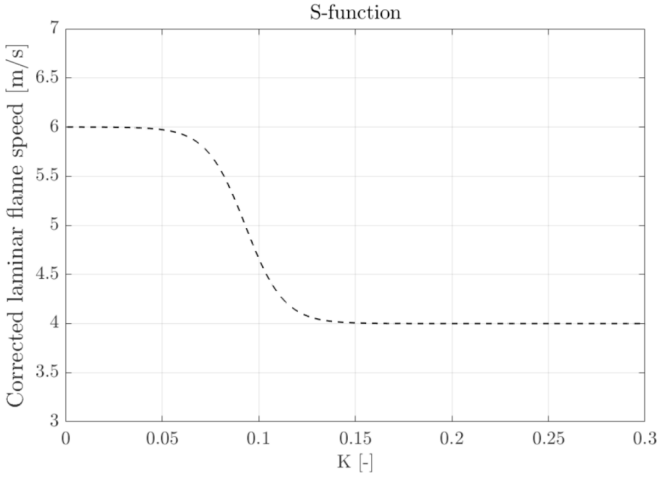

Fig. 4. S-function behavior as a function of the Karlovitz stretch factor K. As an example, values of LFS equal to 4 and 6 m/s are considered for the blending.

3.2.6. Concluding remarks

In order to conclude the section dedicated to the numerical setup, some comments are proposed in the following.

First of all, it is important to note that Eqs. (6)–(11), except for Eq. (7), are manually implemented in the software through external Fortran user-coding. The laminar flame speed polynomial correlation and the entire ignition model are implemented via external routines as well. As for Eq. (7), it is used in a Python script in conjunction with a kinetic solver (namely Cantera) to generate a table of ω_2 values. These are then used by Eq. (8), within the turbulent flame speed computation routine, to correct the unstretched laminar flame speed. No further fundamental change is made to the remaining equations.

In general, the combustion framework adopted here (intended as combination of ignition, combustion and quenching models, and turbulent flame speed correlation) is well-consolidated for stable premixed (or partially-premixed) flames, thus it can be extended in principle to any traditional fuel. In this regard, it is useful to remember that some tuning parameters such as the turbulent flame speed constant (set to 3.3 in this case) and the threshold kernel radius that governs the transition from ignition to combustion model (set to 2 mm here) may require fuel-to-fuel calibration. Additionally, the laminar flame speed must be adjusted to reflect the characteristics of the chosen fuel.

Then, in this work, additional sub-models are introduced to include the peculiarities of ultra-lean H_2 combustion. In particular, the laminar flame speed correction to account for the TD instability effect is adopted. Although the methodology for computing ω_2 is fuel-agnostic, the correlation between $\frac{S_{L\,instab}}{S_L}$ and ω_2 is fuel-dependent. Therefore, this correlation is specific for ultra-lean H_2 combustion and not directly applicable to other fuels. Also, the approach for the turbulence-instability interaction based on the Karlovitz stretch factor is fuel-agnostic. Even if it is purposely introduced to compare the effect of the H_2 TD instabilities to the turbulence one, it can be adopted in principle with any fuel.

3.3. Mesh

The adopted mesh is chosen following a sensitivity analysis, whose details can be found in [31]. The grid is a compromise between computational cost and grid-independency of the results, i.e. further refinements do not lead to remarkable modifications of the simulation outcomes. The cell size adapts to the local geometry, ranging between 0.6 and 1.2 mm. Furthermore, a single prismatic layer of 0.3 mm is applied on each wall. The number of cells at the bottom dead center (BDC) is roughly 600 k. The adopted mesh is shown in Fig. 5.

4. Results

Due to the adopted boundary conditions, the in-cylinder mixture is perfectly homogeneous. Therefore, no investigation on cold flow and mixing is presented in this paper and the result section focuses on combustion-related aspects.

Firstly, a numerical-experimental comparison in terms of in-cylinder pressure is shown for the 'base' numerical setup, namely without instability, turbulence-instability interaction and quenching at walls. Secondly, the outcomes obtained including the flame instability are discussed and the impact of the instability is highlighted. Thirdly, the turbulence-instability interaction is included. Finally, the wall flame quenching is added and the result obtained with the 'improved' setup are compared with the previous ones. Also, the comparison against the experiments is deepened at this final stage.

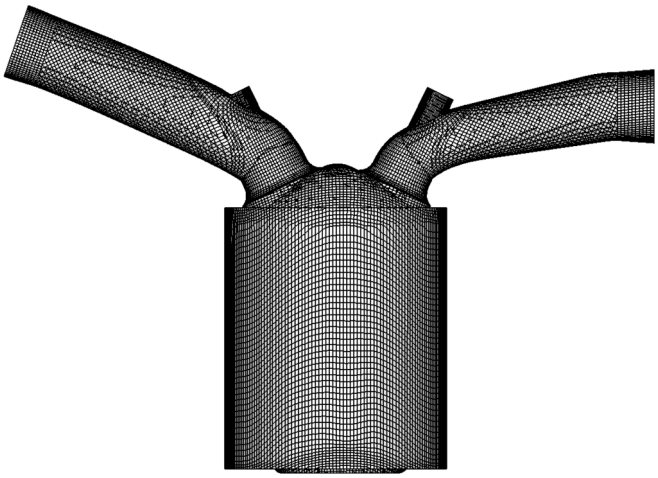

Fig. 5. The adopted computational grid at the BDC.

4.1. 'Base' setup results

Before the presentation of the 'improved' setup results, it is necessary to focus the attention on the 'base' one and discuss its applicability, especially focusing on the combustion model. Surprisingly, G-equation properly performs throughout the conditions without any case-to-case calibration. This is not straightforward considering the wide range of conditions encountered in the investigated cases. In this regard, Fig. 6 shows the Borghi-Peters diagram, commonly adopted to classify the combustion regime. $\frac{u'}{S_L}$ and $\frac{l_t}{\delta}$ computed as mass average on the cells involved in the flame front are reported during combustion, for each operating point. As visible in Fig. 6, the investigated operating conditions span all over the combustion regimes. Therefore, a case-to-case calibration of the combustion model may be expected, in order to compensate for the fact that it is working out of range (i.e. flamelet regime). The unfulfilled expectation can be explained by recovering the Lewis number. Interestingly, one of the assumptions of the proposed diagram is Lewis number equal to 1 [68], i.e. the proposed regime classification is valid as long as the mixture Lewis number is close to 1.

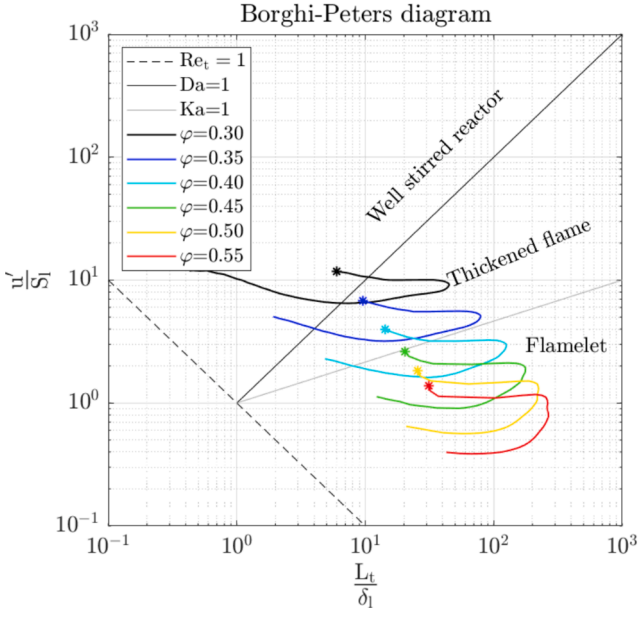

Fig. 6. Borghi-Peters diagram for the investigated cases. Each line represents the evolution (averaged on the flame front) of the regime during combustion. These results are obtained from the 'base' setup simulations.

However, especially at extremely lean conditions, hydrogen mixtures show a much lower value. This significant deviation makes the use of the Borghi-Peters diagram, as it is, debatable. In other words, if a hydrogen flame lays in the 'well-stirred reactor' regime region of the diagram, as it happens for the leanest case, it is not necessarily true that the actual combustion regime corresponds to that one. As a demonstration, in a previous work [69], the authors of the present paper were able to clearly distinguish the presence of a hydrogen flame, although the combustion regime was formally 'well-stirred reactor'. Therefore, the adoption of a flamelet combustion model may be appropriate.

In Fig. 7a and b, the results in terms of average in-cylinder pressure and apparent heat release rate (AHRR) obtained with the 'base' setup are presented along with the experiments. Except for minor deviations, the overall agreement is satisfactory. This indicates that, although some combustion-related phenomena (such as TD instability) are neglected at this stage, the modeling framework is able to accurately capture the main trends across the different cases anyway.

4.2. Thermo-diffusive instability addition

Starting with the 'base' setup refinement, the effect of the TD instability is introduced. Fig. 8 reports numerical and experimental in-cylinder pressure, for each case. With respect to the 'base' setup (whose results are added in Fig. 8 for comparison), the predicted pressure traces are moderately affected by TD instability. To explain this behavior, the numerical traces are colored by the increment ($S_{Linstab}/S_L$) that the unstretched LFS undergoes when corrected, according to Eq. (8), and they are reported in Fig. 9. Coherently with the existing literature, the impact of the TD instability is strong for very lean mixtures. However, it is remarkable only towards the end of combustion, when the unburnt temperature decreases (i.e. when the stabilizing effect of temperature is less and less able to compensate the destabilizing one of pressure). Therefore, the effect on performance, namely in-cylinder pressure, is limited. It should be noted that if the combustion is fast enough, the end of the process is reached early in the power stroke, i.e. when the unburnt temperature is still high. This is the reason why the instability effect weakens rapidly, moving from φ = 0.30 to φ = 0.55. In other words, the instability impact reduces twice when moving towards stoichiometry. Firstly, because of the effect of the equivalence ratio, as highlighted by the proposed maps in Fig. 3. Secondly, because the combustion ends sooner in the power stroke, i.e. when the unburnt temperature is higher and the stabilizing effect results stronger.

By comparing Figs. 8 and 9, it is possible to notice that the effect of instability on the pressure traces is comparable, although the LFS correction is strongly different for the cases. This is evident by comparing, for instance, φ = 0.30 and φ = 0.55. The reason is triple. Firstly, the pressure values of the traces are very different, so a similar variation in absolute terms implies a significantly different variation in percentage. Therefore, the pressure modification for the leanest cases is higher. Secondly, an increase in LFS does not correspond to an equal increase in turbulent flame speed, which is much lower. Therefore, significant variations of laminar flame speed do not correspond to similarly large variations of burn rate and in-cylinder pressure. Thirdly, the instability effect manifests towards the combustion end, when the heat release rate is already low and any acceleration of it does not relevantly affect the pressure trace.

Finally, again comparing Figs. 8 and 9, it is evident that the effect of instability on in-cylinder pressure does not match, in terms of phasing, the peak of laminar flame speed correction. For instance, considering φ = 0.40 case, the pressure rise is concentrated in the first part of the combustion, when the LFS correction is lower. The reason is that both laminar flame speed and its correction are great enough to lead to a visible effect on the in-cylinder pressure trace at the beginning of the combustion. Moving towards the end of the process, LFS is much more accelerated but, similarly to the above, the effect becomes difficult to observe, due to the low heat release rate during the combustion

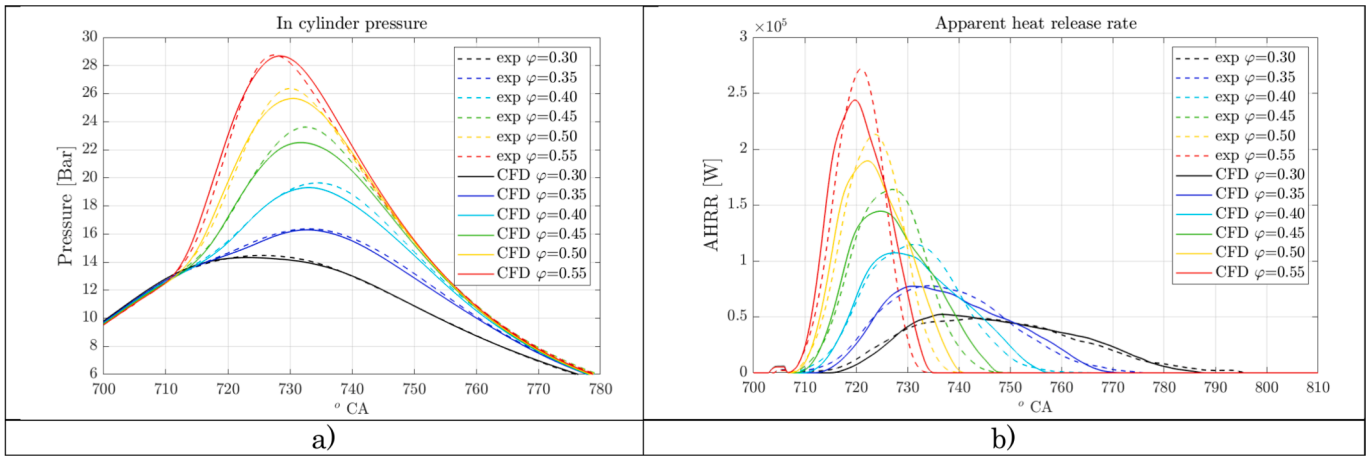

Fig. 7. Numerical-experimental comparison in terms of in-cylinder pressure (a) and AHRR (b), for each investigated condition. CFD results are obtained with the 'base' setup.

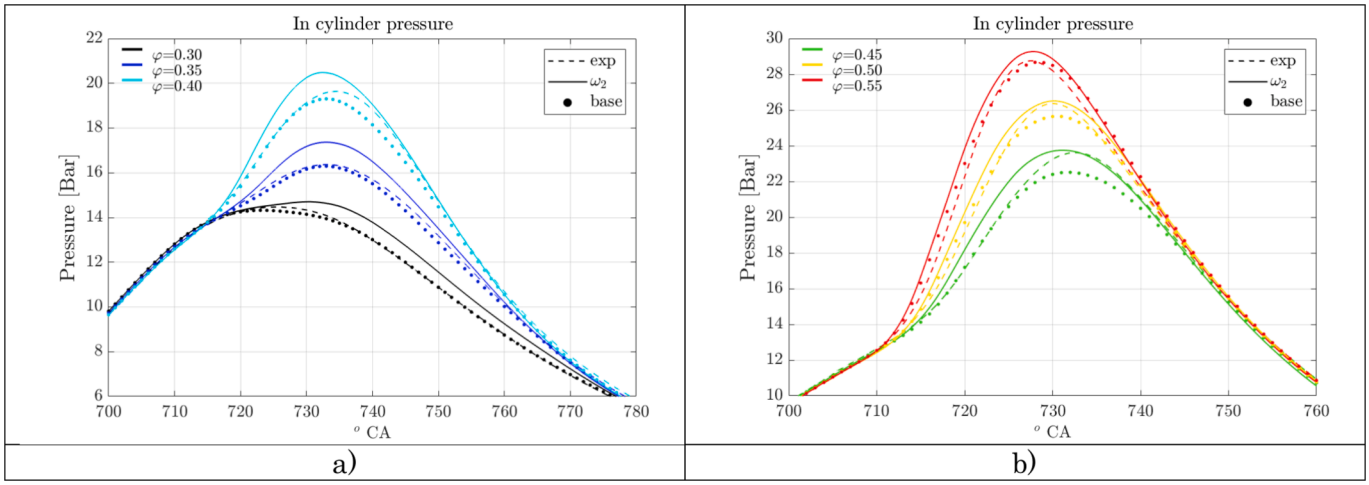

Fig. 8. Numerical-experimental comparison in terms of in-cylinder pressure, for each investigated condition. Two sets of CFD results are presented, i.e. ones obtained with the 'base' setup (Base) and ones obtained with the 'base' setup with the addition of the TD instability effect (ω_2). The sweep is split in two figures, (a) and (b), for improved readability.

completion.

In order to better appreciate the effect of the TD instability compared to the 'base' setup, experimental and numerical AHRRs are reported in Fig. 10. It is possible to observe that, compared to the CFD outcomes proposed in Fig. 7b, all the predicted combustions are now shorter and their phasing is advanced. As for the leaner cases, also the combustion end is particularly anticipated compared to the experimental counterpart.

A final observation concerns the applicability of the instability correction factor within a URANS framework. The turbulence-induced variability contributes to cycle-to-cycle differences not only by means of the unstretched laminar flame speed (which varies with the thermodynamic conditions), but also by the TD instability itself (which depends on the thermodynamic conditions as well). This further amplifies the spread of the pressure traces between the cycles. The question is if the calculation of the TD instability effect for the average cycle calculated by the URANS approach makes sense. In fact, faster-burning cycles may be influenced by TD instability differently compared to slower-burning ones. Therefore, although the experimental cycles are averaged using a simple linear method, the flame speed predicted by the URANS approach for a single representative cycle does not necessarily correspond to the flame speed of the linearly-averaged experimental cycle. Nevertheless, the URANS approach remains meaningful because, in premixed combustion cases like the investigated ones, the thermodynamic conditions at a given crank angle slightly vary from cycle to cycle. As a result, the corresponding laminar and turbulent flame speeds modify almost linearly between the cycles. The same is valid also for the TD instability contribution. Although it introduces further non-linear effects, the limited differences between the thermodynamic conditions of the cycles lead to variations of the instability contribution that can be approximated as linear. Moreover, the opposed influences of pressure and temperature on the TD instability correction factor help to limit its variation across the different engine cycles. In order to prove this, Fig. 11 presents the scatter of the experimental pressure traces for the $\varphi = 0.30$ case, purposely selected as it is the one with the highest cycle-to-cycle variability. The pressure traces of two URANS cycles are reported as well, aiming at mimicking the slower and the faster experimental cycles by the adjustment of the spark timing. This method is used coherently with the origin of the cycle-to-cycle variability for this operating point. In fact, it is mainly originated during the early stage of combustion, by the variability of the flow field at the spark. This is confirmed by a dedicated LES analysis which is currently ongoing on the operating point. The CFD traces are colored by the laminar flame speed correction factor, which shows similar values for the two curves. Therefore, for each crank angle, the variation of the TD instability effect (i.e. the variation of the correction factor) can be reasonably assumed as

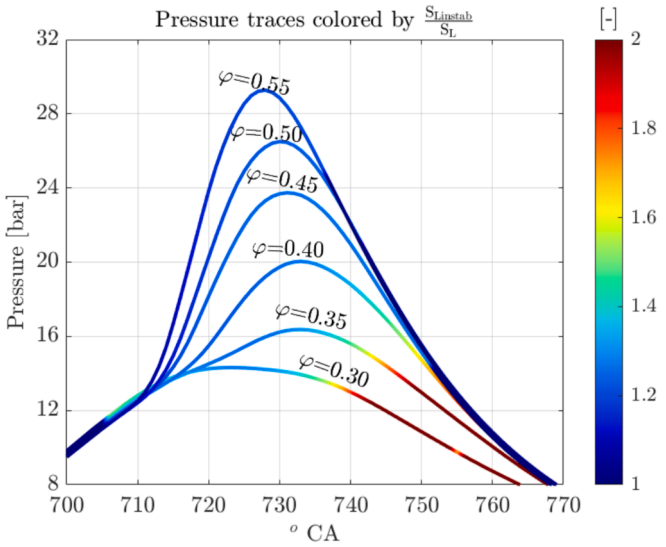

Fig. 9. Computed pressure traces colored by the average percentage correction to the unstretched laminar flame speed. For completeness, pressure traces are colored from mass of fuel burnt (MFB) 0 to MFB 99.

linear.

4.3. Karlovitz stretch factor addition

The Karlovitz stretch factor is now introduced to consider the interaction between TD instability and turbulence. In particular, it allows to distinguish the cases in which the TD instability has an impact (i.e. it is possible to recognize its effect) from those in which it is negligible, with respect to turbulence. The mass-averaged value assumed by this parameter on the flame front cells is plotted in Fig. 12, during combustion, for each case.

The combination of threshold suggested by Bradley ($K = 0.1$) and S-shaped function splits the cases in three groups. The first one includes $\varphi = 0.30$ and $\varphi = 0.35$ and it is characterized by a chemistry that is so slow that the instability-induced wrinkling is secondary compared to the one due to turbulence. $\varphi = 0.45$, $\varphi = 0.50$ and $\varphi = 0.55$ pertain to the second group, in which the actions of both instability and turbulence coexist. The third group comprises the remaining case, namely $\varphi = 0.40$, which is characterized by K values that move across the threshold, thus undergoing the effect of the S-function. In this regard, it is necessary to point out that, based on the adopted values for the parameters governing center and width, the S-shaped function mainly acts on the $\varphi = 0.40$ case, while the impact on $\varphi = 0.45$, $\varphi = 0.50$ and $\varphi = 0.55$ ones is negligible. In the light of these clarifications, $\varphi = 0.45$, $\varphi = 0.50$ and $\varphi = 0.55$ cases are mainly characterized by the use of $S_{Linstab}$, while S_L is mostly adopted by the code for $\varphi = 0.30$ and $\varphi = 0.35$ simulations. Finally, $\varphi = 0.40$ case rely on a blend of the two flame speeds. The results in terms of in-cylinder pressure obtained by introducing the effect of the Karlovitz stretch factor are presented in Fig. 11. In order to highlight the effect of K, in the same figure also the results without it are reported. In Fig. 13a, it is evident that K acts in $\varphi = 0.30$, $\varphi = 0.35$ and $\varphi = 0.40$ cases. Moreover, by comparing Figs. 13 and 7a, it is possible to notice that, due to the action of K, the instability effect is de facto neglected at $\varphi = 0.30$ and $\varphi = 0.35$, while it is still visible in the other ones. As for the

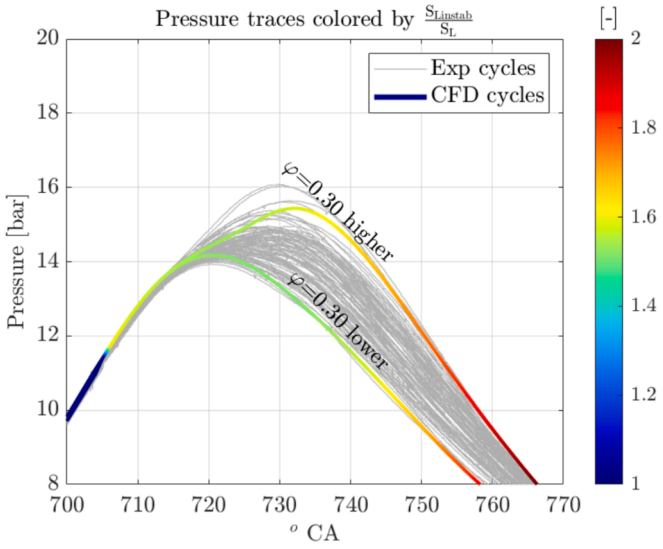

Fig. 11. Scatter of the experimental cycles for $\varphi = 0.3$ case. Two CFD cycles colored by the laminar flame speed correction factor are reported as well.

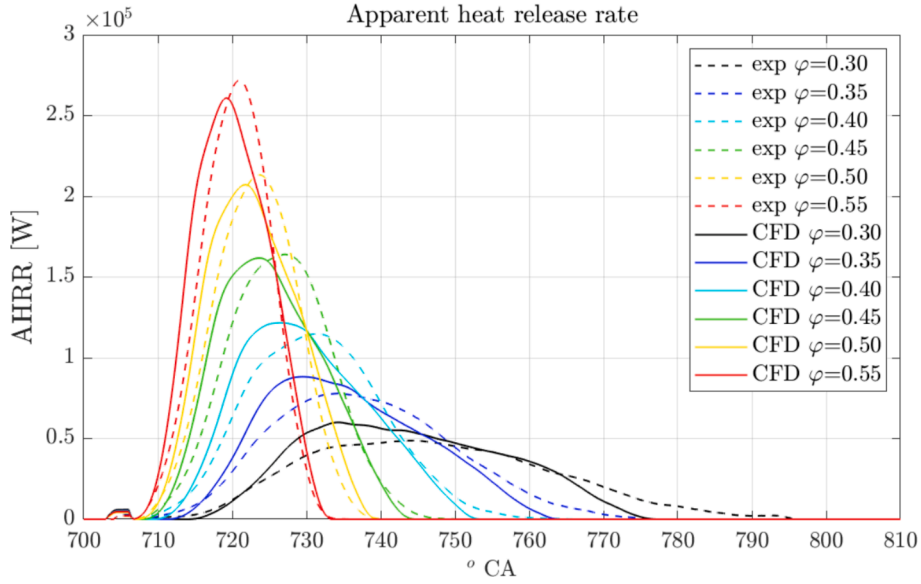

Fig. 10. Comparison in terms of AHRR between CFD and experiments. CFD results are obtained with the 'base' setup with the addition of the TD instability effect (ω_2).

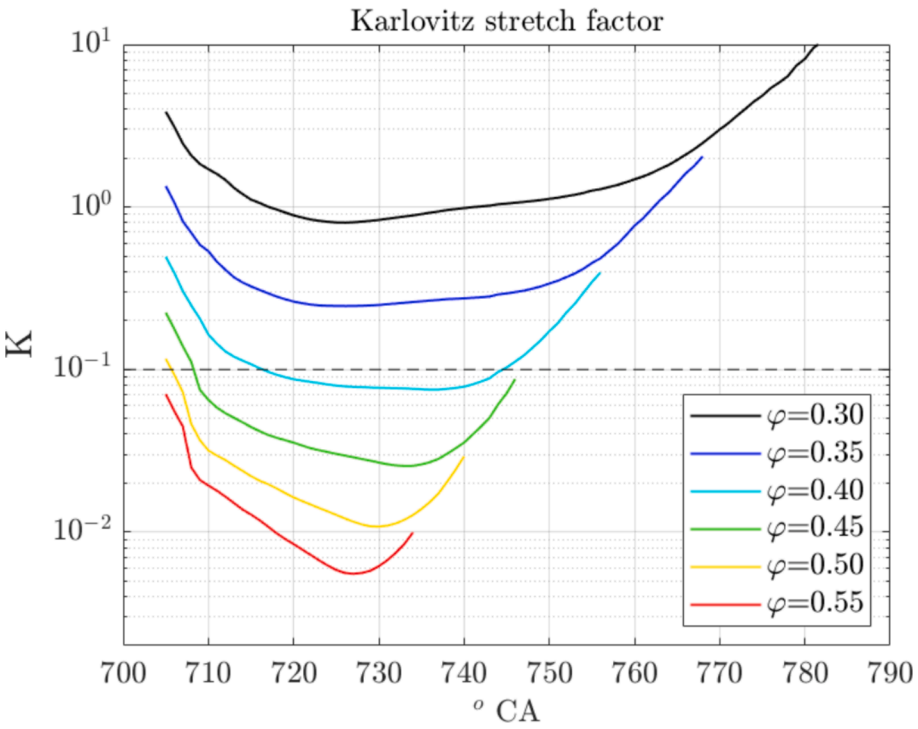

Fig. 12. Mass-averaged Karlovitz stretch factor on the flame front cells, during combustion, for all the cases.

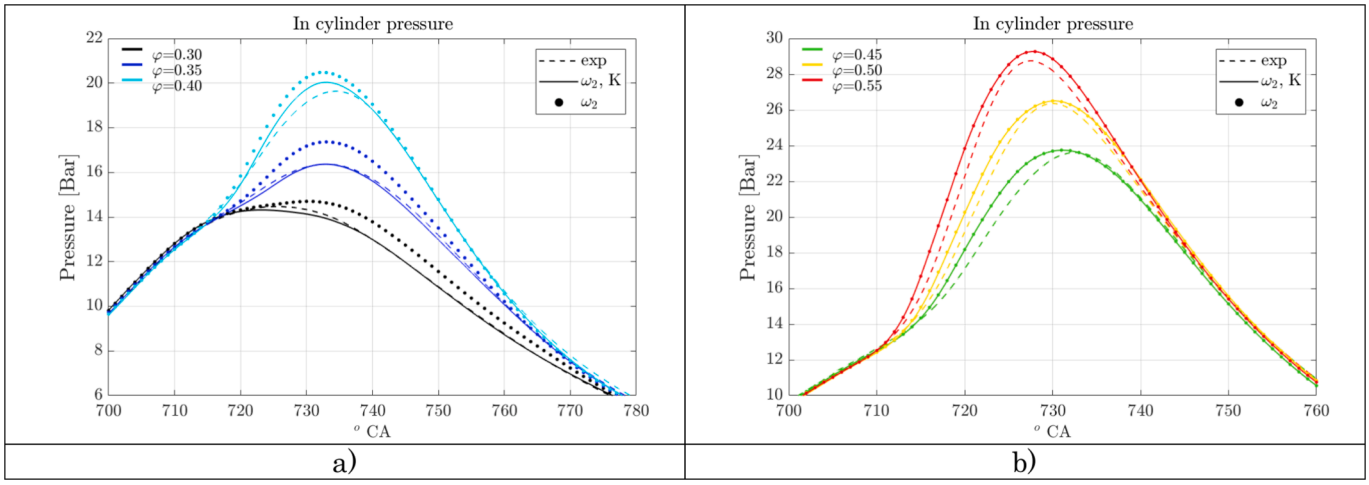

Fig. 13. Numerical-experimental comparison in terms of in-cylinder pressure, for each investigated condition. Two sets of CFD results are presented, i.e. ones obtained with the 'base' setup with the addition of the TD instability effect (ω_2) and the ones obtained with 'base' setup and adding the effect of both TD instability and Karlovitz stretch factor (ω_2, K). The sweep is split in two figures, (a) and (b), for improved readability.

$\varphi = 0.40$ case, the pressure trace is characterized by values that are lower compared to the previous setup ('base' with instability effect) but higher with respect to the 'base' one, which demonstrates the action of the S-shaped function.

Fig. 14 reports the numerical AHRR traces, obtained with the setup including TD instability effect and K, and the experimental ones. AHRR traces allow to point out the benefits related to the introduction of K. The agreement improvement is confirmed for $\varphi = 0.30$, $\varphi = 0.35$ and $\varphi = 0.40$ cases. As shown in Fig. 10, in fact, the adoption of the TD instability effect alone is strongly penalizing for these cases. As for the remaining ones, K does not act and no difference can be noticed between Figs. 10 and 14.

As previously mentioned, there are two parameters defining the S-function, equal to 100 and 0.1, respectively. The first one determines the slope of the S-curve and it is used as a calibration parameter. The second one corresponds to the threshold value of K. It is inherited from the literature, and it is not varied in this analysis. To assess the sensitivity to the slope, additional simulations are performed with values equal to 50 and 10000. As visible in Fig. 15, varying this parameter alters the sharpness of the transition, thus affecting how quickly the laminar flame speed changes (from S_L to $S_{Linstab}$) for the cases whose K is close to the threshold.

The sensitivity analysis is conducted only for $\varphi = 0.35$, $\varphi = 0.40$ and $\varphi = 0.45$ cases, as these are the ones falling, on average, close to the $K = 0.1$ threshold. Fig. 16 shows the pressure traces for these cases using the three different S-function slopes. The impact is minimal, and only the case closest to the threshold, i.e. $\varphi = 0.40$, is affected. The effect on it is to slightly inflate the pressure trace, as a consequence of the sharp

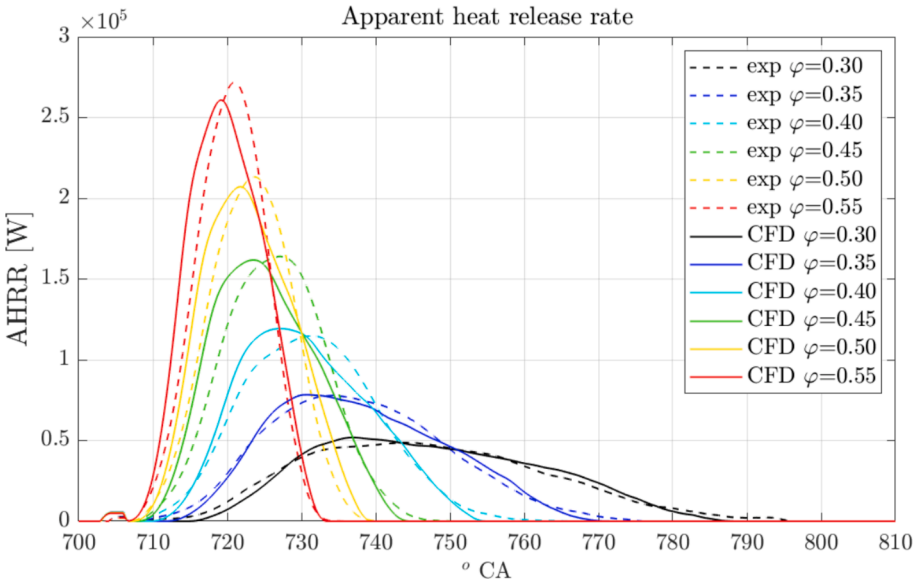

Fig. 14. Comparison in terms of AHRR between CFD and experiments. Results are obtained with the 'base' setup and adding the effect of both TD instability and Karlovitz stretch factor.

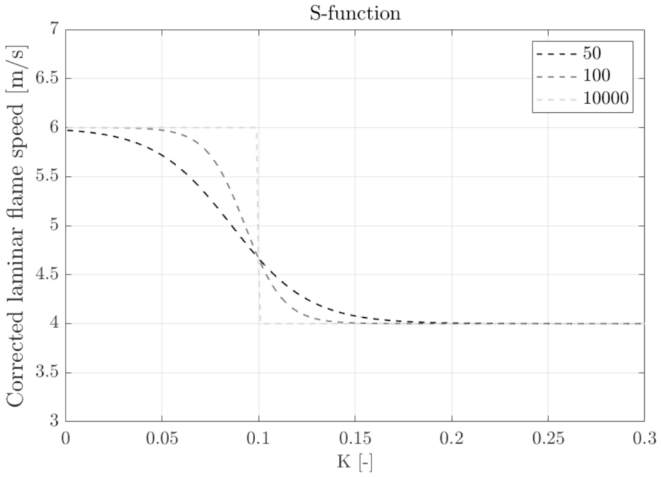

Fig. 15. S-function sensitivity to the slope.

transition between the regimes that allows for advanced onset of instability. On the other hand, φ = 0.35 case remains almost completely confined in the fully turbulent regime, while the φ = 0.45 case is almost entirely affected by TD instability during all the cycle.

4.4. Wall quenching addition ('Improved' setup)

As a final step of setup refinement, the wall flame quenching sub-model is introduced. The results obtained with the final framework including all the sub-models are reported in Fig. 17, in terms of average in-cylinder pressure, along with experiments and results obtained without quenching. As visible, the introduction of flame quenching leads to minimal variations of the results. The pressure peaks of φ = 0.50 and φ = 0.55 cases slightly improve, as the instability effect is partly compensated. As for φ = 0.30 and φ = 0.35, the quenching effect causes a weak underestimation of the of experimental trace during the expansion stroke. Despite this negative aspect, the effect on the apparent heat release rate (AHRR) tail is positive, as it will be pointed out in the following.

By comparing Fig. 14 with Fig. 7, it can be noted that the results of the 'base' and 'improved' setups are similar. This means that prevailing turbulence effects and wall quenching of the flame roughly compensate the impact of the TD instability. However, compared to the 'base' setup, an improvement in the peak pressure prediction is visible, especially for φ = 0.45 and φ = 0.50 cases.

To better describe the results achieved with the final ('improved') version of the setup and point out the predictive capabilities (as no case-by-case calibration is carried out), the numerical results in terms of AHRR and combustion indicators are compared with the experiments. Fig. 18 reports a comparison between CFD and experiments in terms of AHRR, for each case. A good agreement is noticed, especially for the combustion completion, thanks to the action of both instability and quenching. In particular, φ = 0.30 and φ = 0.35 are characterized by the action of the flame quenching that extends the AHRR tail and allows a close agreement with the experiments to be obtained. As for the other cases, apart from quenching, the TD instability is present, leading to a progressive shortening of the tail, visible also in the experiments. The correct modeling of the combustion completion also represents an improvement compared to the 'base' setup. However, there is still room for amelioration. In fact, a slight overestimation of the combustion rate in the first half of the process can be noted, along with a progressively delayed AHRR growth moving to lean mixtures, attributable to the ignition model. In this regard, for a proper comparison, no recalibration of ignition and combustion model parameters is carried out moving from 'base' to 'improved' setup. A recalibration of the models may lead to further improvements of the results. It is interesting to point out that the small spikes observed at 705° CA result from the initialization of G-equation, which leads to the formation of an initial burnt mass. Such an initialization is a modeling requirement, even though the effective propagation of G begins later, following the delay imposed by the ignition model.

Fig. 19 shows a numerical-experimental comparison of combustion indicators, which provide a more quantitative description of the results discussed above in terms of AHRR. An overall satisfying agreement between CFD and experimental outcomes is noticed. In detail, Fig. 19a shows the MFB 0–10, which confirms that, moving to leaner mixtures, the lengthening of the combustion initiation is slightly overpredicted by the simulations. Fig. 19b reports the MFB 50 and, even in this case, the observations on the AHRR are confirmed. The overprediction of the combustion rate in the first half of the process results in a slight underestimation of the combustion phasing. As for the duration (namely

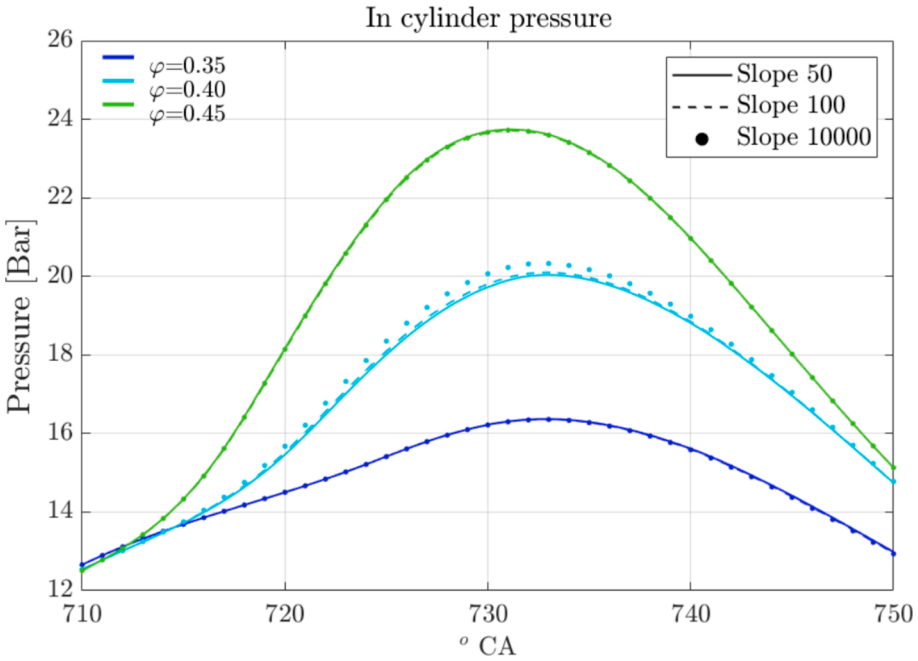

Fig. 16. Sensitivity of the CFD pressure traces to the 'slope' parameter of the S-function, for φ = 0.35, φ = 0.40 and φ = 0.45 cases.

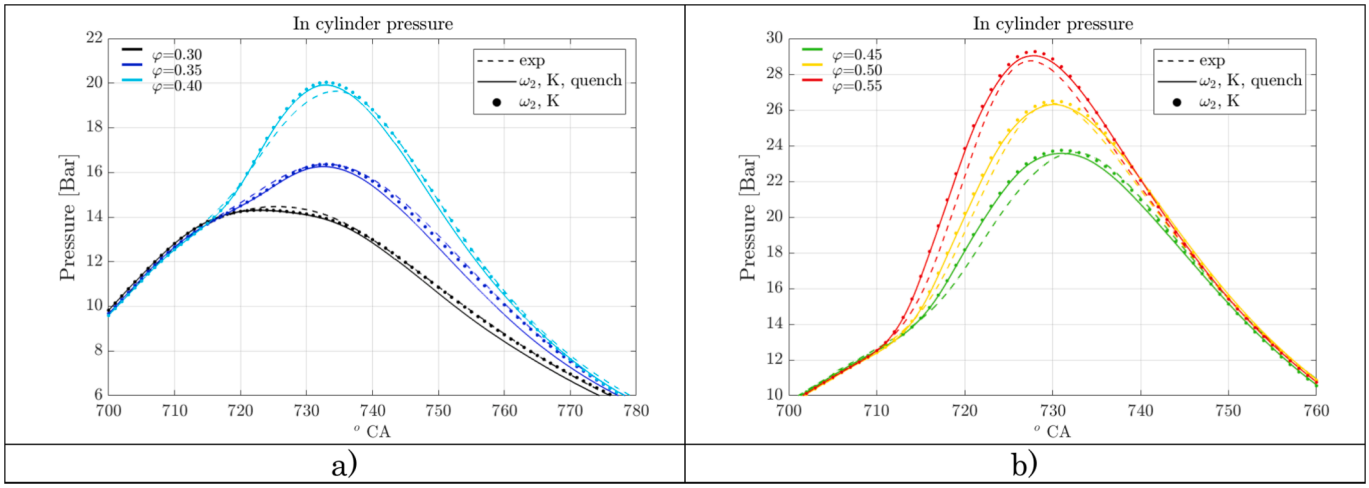

Fig. 17. Numerical-experimental comparison in terms of in-cylinder pressure, for each investigated condition; two sets of CFD results are presented, i.e. ones obtained with 'base' setup and the effect of both TD instability and Karlovitz stretch factor (ω_2 K), and ones obtained with the 'improved' framework, featuring all the sub-models (ω_2 K quench). The sweep is splitted in two figures, (a) and (b), for improved readability.

MFB 10–90), Fig. 19c confirms an overprediction of the experiments for all the cases, which is probably due to an overestimation of the quenching effect. However, similarly to the other indicators, the error in the MFB 10–90 prediction is still acceptable.

Thanks to the outcomes of the proposed simulation framework, it is possible to point out the moderate influence of the TD flame instability and the capability of turbulence-instability interaction and wall quenching to perfectly compensate it. The limited impact of the flame instability is a noteworthy outcome of this work. In fact, following the existing literature [20,61,70], the selected operating points presenting extremely lean mixtures and low revving speed should be characterized by a significant effect of the TD instability, that increases the flame speed despite low turbulence. However, pressure and temperature also play an important role and, at the investigated engine-like conditions, the stabilizing effect of the temperature limits the impact of the TD instability.

As a further remark on the results, it is useful to point out the proven predictive capabilities of the proposed numerical framework, especially of the turbulent flame speed correlation and, more in general, of the combustion model. In fact, the investigated conditions cover a wide range of the $\frac{u'}{S_L}$ ratio. The different values are obtained keeping u' roughly constant (as the engine speed does not modify), while changing the laminar flame speed through the variation of the mixture quality. The $\frac{u'}{S_L}$ sweep is particularly relevant not only for the wide range of φ (including conditions potentially affected by TD instability), but also with respect to the turbulent flame speed correlation, which depends solely on $\frac{u'}{S_L}$ itself. A wide variation of this ratio without case-by-case calibration strengthens the robustness of the combustion model, demonstrating the validity of the correlation across very different operating conditions.

Finally, it is possible to conclude that all the proposed results represent an advancement compared to the state of the art provided by the literature dealing with TD instability modeling. For instance, both Hernandez et al. [19] and Ramognino et at [17] only study the effect of

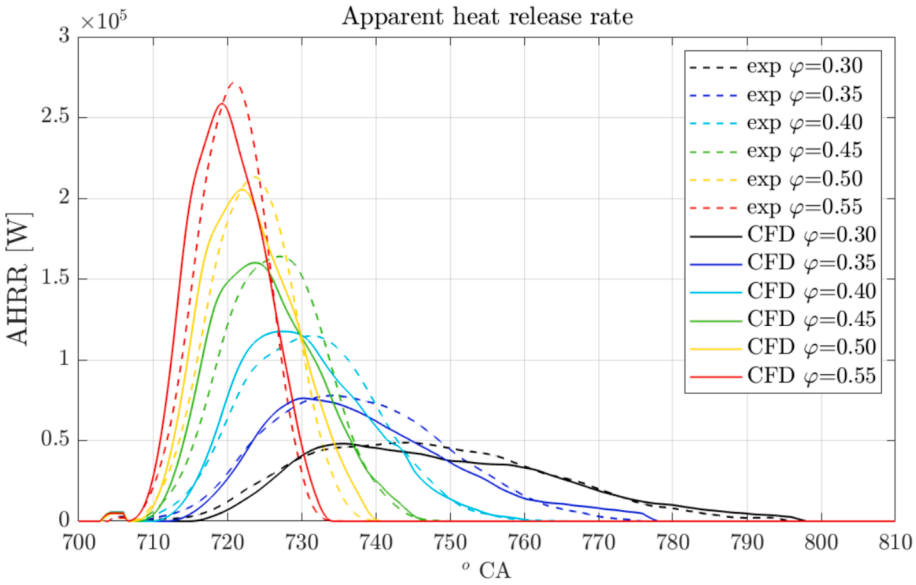

Fig. 18. Numerical-experimental comparison in terms of AHRR, for each investigated condition; CFD results are obtained with the 'improved' setup, featuring all the sub-models.

laminar flame speed but neither wall flame quenching nor turbulence-instability interaction are considered. Moreover, in both the works a DI engine is investigated. Although an accurate validation is carried out, uncertainties relative to the stratification remain, which are completely eliminated in the present work. While Ramognino et al. show significant impact of the TD instability, in the work of Hernandez et al. [19], only a slight modification of the pressure traces is observed, similarly to the present paper. Overall, compared to [17] and [19], the present work shows higher accuracy of the numerical outcomes with respect to the experiments, and the validation is carried out on a wider set of conditions. On the other hand, Novella et al. [21] include a quenching model and investigate a PFI engine unaffected by mixture inhomogeneities, as in this work. They notice a stronger effect of TD instabilities at $\varphi = 0.30$. However, this does not necessarily contradict the findings of the present paper, as pressure and temperature conditions differ significantly. Additionally, the turbulence-instability interaction is not considered in [21]. Therefore, this represents a key contribution of the current work to the existing literature. Finally, compared to [21], higher accuracy of the CFD results can be noticed in the present paper.

5. Conclusions

A 3D-CFD framework for in-cylinder simulations of H_2 ICEs is proposed. The setup includes the modeling of TD instability, turbulence-instability interaction and wall quenching of the flame, among other things. It is validated against experimental data on multiple operating conditions characterized by a wide range of equivalence ratios. The framework is able to properly predict engine performance and, thus, it can be exploited by designers to develop new generations of H_2 ICEs.

The numerical setup is firstly presented in a 'base' version, inherited from a previous work by the authors. Then, step-by-step, it is refined by including sub-models to consider the effect of TD instability, turbulence-instability interaction (through the Karlovitz stretch factor) and wall quenching of the flame. Compared to the 'base' setup, the 'improved' version (i.e. the one including all the sub-models) shows similar results. In other words, the instability effect is canceled out by considering the prevailing effect of turbulence and wall flame quenching. In particular, at higher equivalence ratio values, the instability impact is minimal and partly compensated by the action of the flame quenching. In the leanest cases, where the instability reaches a maximum, the effect is mainly inhibited by the Karlovitz stretch factor.

Apart from the proposal of a comprehensive framework, the present paper offers a deepening into the effect of the TD instability. At the investigated conditions, the impact is not negligible, but not even significant. The reason is explained by the proposed values of ω_2, a parameter determining the instability growth rate due to TD effects. High ω_2 values (i.e. strong instability) are obtained with low unburnt temperature, while the dependency on pressure and equivalence ratio is more complex. This means that the effect of the instability has to be evaluated case by case. Based on the thermodynamic conditions of the investigated operating points, LFS correction is significant only for the leanest cases. However, even for them, the impact of the instability is limited. In fact, the thermodynamic conditions promoting the TD instability are achieved only towards the combustion end.

Since the investigated engine is PFI, the drawn conclusions are not affected by uncertainties related to the mixture stratification. In this regard, it is necessary to remind that the proposed approach is strictly valid for premixed combustion. From a purely numerical standpoint, it can be applied also to DI engines with stratified mixture, as in [17] and [19]. In that case, the laminar flame speed correction factor is still applied across the entire flame surface, but the correction also depends on the local φ besides p, T and EGR. However, this is a simplified approach as the mutual interaction between TD instability, turbulence and mixture inhomogeneity is more complex, as shown in [71]. Therefore, the applicability to stratified mixtures requires rigorous validation, which is beyond the goal of the present study.

It is important to point out that, although the instability effect is minimal for the investigated cases, different engine operating conditions may manifest a stronger impact. For this reason, as a future development, other operating conditions and/or engines will be investigated. Finally, as for the turbulence-instability interaction, it will be necessary to refine the superimposition method and improve the approach to interaction by considering the characteristic scales of eddies and flame instabilities.

CRediT authorship contribution statement

Stefano Sfriso: Writing – original draft, Validation, Methodology, Investigation, Formal analysis. **Fabio Berni:** Writing – review & editing, Supervision, Methodology, Investigation. **Sebastiano Breda:** Writing – review & editing, Supervision, Methodology, Investigation. **Caio Ramalho Leite:** Writing – review & editing, Investigation, Data curation,

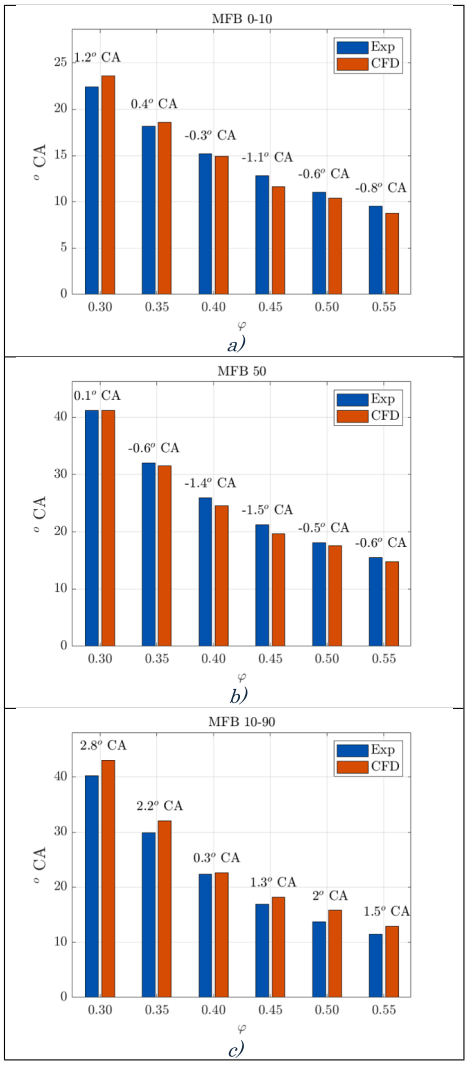

Fig. 19. Numerical-experimental comparison in terms of combustion indicators, for each investigated condition; CFD results are obtained with the 'improved' setup, featuring all the sub-models; (a) MFB 10, (b) MFB 50 and (c) MFB 10–90.

Conceptualization. **Fabriche Foucher:** Supervision, Data curation, Conceptualization. **Pierre Bréquigny:** Writing – review & editing, Supervision, Data curation. **Jacques Borée:** Supervision, Data curation. **Stefano Fontanesi:** Writing – review & editing, Supervision, Methodology.

Declaration of competing interest

The authors declare that they have no known competing financial interests or personal relationships that could have appeared to influence the work reported in this paper.

Acknowledgments

The experimental work described in this paper has been conducted by Caio Ramalho Leite, Pierre Brequigny and Fabrice Foucher from the University of Orléans, and Jacques Borée from the ISAE-ENSMA.

The authors gratefully acknowledge the University of Modena and Reggio Emilia for supporting the activity by the "Fondo di Ateneo per la Ricerca 2024 per il finanziamento di piani di sviluppo dipartimentale nell'ambito della ricerca" (FARD 2024-2025), the Agence Nationale de Recherche for the grant number 20-CE05-0007 (ALEKCIA ANR project) and the PIANO NAZIONALE DI RIPRESA E RESILIENZA (PNRR) – MISSIONE 4 COMPONENTE 2, "Dalla ricerca all'impresa" INVESTIMENTO 1.4, Potenziamento strutture di ricerca e creazione di "campioni nazionali di R&S" su alcune Key Enabling Technologies, finanziato dall'Unione Europea – NextGenerationEU – Progetto identificato con codice CN00000023. Titolo "Sustainable Mobility Center (Centro Nazionale per la Mobilità Sostenibile – CNMS)" – Spoke 12 – Avviso MUR 3138/2021 modificato con DD 3175/2021".

Data availability

Data will be made available on request.

References

[1] Regulation (EU) 2023/851 of the European parliament and of the council. Off J Eur Union, OJ L 110.
[2] Larson ED. A review of life-cycle analysis studies on liquid biofuel systems for the transport sector. Energy Sustain Dev 2006;10(2):109–26. https://doi.org/10.1016/S0973-0826(08)60536-0.
[3] Das L. Exhaust emission characterization of hydrogen-operated engine system: nature of pollutants and their control techniques. Int J Hydrogen Energy 1991;16(11):765–75. https://doi.org/10.1016/0360-3199(91)90075-T.
[4] Bekdemir C, Doosje E, Seykens X. H2-ICE technology options of the present and the near future; 2022. https://doi.org/10.4271/2022-01-0472.
[5] Millo F, et al. Synergetic application of zero-, one-, and three-dimensional computational fluid dynamics approaches for hydrogen-fuelled spark ignition engine simulation. p. 03-15-04-0030 SAE Int J Engines 2021;15(4). https://doi.org/10.4271/03-15-04-0030.
[6] Zhang Y, Mathieu O, Petersen EL, Bourque G, Curran HJ. Assessing the predictions of a NO x kinetic mechanism on recent hydrogen and syngas experimental data. Combust Flame 2017;182:122–41. https://doi.org/10.1016/j.combustflame.2017.03.019.
[7] Liu X, et al. Hydrogen pre-chamber combustion at lean-burn conditions on a heavy-duty diesel engine: a computational study. Fuel 2023;335:127042. https://doi.org/10.1016/j.fuel.2022.127042.
[8] Babayev R, Andersson A, Dalmau AS, Im HG, Johansson B. Computational characterization of hydrogen direct injection and nonpremixed combustion in a compression-ignition engine. Int J Hydrogen Energy 2021;46(35):18678–96. https://doi.org/10.1016/j.ijhydene.2021.02.223.
[9] Pielecha I, Merkisz J, Urbański P, Gallas D, Andrych-Zalewska M. A numerical study of the effect of hydrogen fuelled turbulent jet ignition engine. In: SAE technical papers. SAE International; 2022. https://doi.org/10.4271/2022-01-1007.
[10] Rouleau L, Duffour F, Walter B, Kumar R, Nowak L. Experimental and numerical investigation on hydrogen internal combustion engine. In: SAE technical papers. SAE International; 2021. https://doi.org/10.4271/2021-24-0060.
[11] Maio G, et al. Experimental and numerical investigation of a direct injection spark ignition hydrogen engine for heavy-duty applications. Int J Hydrogen Energy 2022;47(67):29069–84. https://doi.org/10.1016/j.ijhydene.2022.06.184.
[12] Knop V, Benkenida A, Jay S, Colin O. Modelling of combustion and nitrogen oxide formation in hydrogen-fuelled internal combustion engines within a 3D CFD code. Int J Hydrogen Energy 2008;33(19):5083–97. https://doi.org/10.1016/j.ijhydene.2008.06.027.
[13] Piano A, et al. Experimental and numerical investigation of abnormal combustion phenomena in high-performance hydrogen direct-injection engine operated in stochiometric conditions. Int J Engine Res 2024. https://doi.org/10.1177/14680874241302562.
[14] Berni F, Pessina V, Teodosio L, d'Adamo A, Borghi M, Fontanesi S. An integrated 0D/1D/3D numerical framework to predict performance, emissions, knock and heat transfer in ICEs fueled with NH3–H2 mixtures: the conversion of a marine diesel engine as case study. Int J Hydrogen Energy 2023. https://doi.org/10.1016/j.ijhydene.2023.09.158.
[15] Kosmadakis GM, Rakopoulos CD, Demuynck J, De Paepe M, Verhelst S. CFD modeling and experimental study of combustion and nitric oxide emissions in hydrogen-fueled spark-ignition engine operating in a very wide range of EGR rates. Int J Hydrogen Energy 2012;37(14):10917–34. https://doi.org/10.1016/j.ijhydene.2012.04.067.
[16] Gerke U, Steurs K, Rebecchi P, Boulouchos K. Derivation of burning velocities of premixed hydrogen/air flames at engine-relevant conditions using a single-cylinder compression machine with optical access. Int J Hydrogen Energy 2010;35(6):2566–77. https://doi.org/10.1016/j.ijhydene.2009.12.064.
[17] Ramognino F, Sforza L, Cerri T, Lucchini T, Onorati A, Novella R. A fast and reliable CFD approach to design hydrogen SI engines for industrial applications. In: SAE technical papers. SAE International; 2023. https://doi.org/10.4271/2023-01-1208.
[18] Berger L, Attili A, Pitsch H. Intrinsic instabilities in premixed hydrogen flames: parametric variation of pressure, equivalence ratio, and temperature. Part 2 – non-linear regime and flame speed enhancement. Combust Flame 2022;240:111936. https://doi.org/10.1016/j.combustflame.2021.111936.
[19] Hernandez I, Turquand D'Auzay C, Penning R, Shapiro E, Hughes J. Thermo-diffusive flame speed adjustment and its application to hydrogen engines. In: SAE

technical papers. SAE International; 2023. https://doi.org/10.4271/2023-01-0197.
[20] Howarth TL, Hunt EF, Aspden AJ. Thermodiffusively-unstable lean premixed hydrogen flames: phenomenology, empirical modelling, and thermal leading points. Combust Flame 2023;253:112811. https://doi.org/10.1016/j.combustflame.2023.112811.
[21] Novella R, Gomez-Soriano J, González-Domínguez D, Olaciregui O. Understanding the role of thermo-diffusive instabilities in hydrogen combustion for lean-burn spark-ignition engine operation. Energy Convers Manag 2025;334:119801. https://doi.org/10.1016/j.enconman.2025.119801.
[22] Howarth TL, Aspden AJ. An empirical characteristic scaling model for freely-propagating lean premixed hydrogen flames. Combust Flame 2022;237:111805. https://doi.org/10.1016/j.combustflame.2021.111805.
[23] Verhelst S, TJoen C, Vancoillie J, Demuynck J. A correlation for the laminar burning velocity for use in hydrogen spark ignition engine simulation. Int J Hydrogen Energy 2011;36(1):957–74. https://doi.org/10.1016/j.ijhydene.2010.10.020.
[24] Zimont VL. Gas premixed combustion at high turbulence. Turbulent flame closure combustion model. Exp Therm Fluid Sci 2000;21(1–3):179–86. https://doi.org/10.1016/S0894-1777(99)00069-2.
[25] Lipatnikov AN, Chomiak J. Turbulent flame speed and thickness: phenomenology, evaluation, and application in multi-dimensional simulations. Prog Energy Combust Sci 2002;28(1):1–74. https://doi.org/10.1016/S0360-1285(01)00007-7.
[26] Gülder ÖL. Turbulent premixed flame propagation models for different combustion regimes. Symp (Int) Combust 1991;23(1):743–50. https://doi.org/10.1016/S0082-0784(06)80325-5.
[27] Sfriso S, et al. Proposal and validation of a numerical framework for 3D-CFD in-cylinder simulations of hydrogen spark-ignition internal combustion engines. Int J Hydrogen Energy 2024;53:114–30. https://doi.org/10.1016/j.ijhydene.2023.12.027.
[28] Sfriso S, Berni F, Fontanesi S, D'Adamo A, Antonelli M, Frigo S. A 3D-CFD Numerical approach for combustion simulations of spark ignition engines fuelled with hydrogen: a preliminary analysis. In: SAE technical papers. SAE International; 2023. https://doi.org/10.4271/2023-01-0207.
[29] Sfriso S, et al. Proposal and validation of 3D-CFD framework for ultra-lean hydrogen combustion in ICEs. In: SAE technical papers. SAE International; 2024. https://doi.org/10.4271/2024-01-2685.
[30] Ramalho Leite C, Laignel M, Brequigny P, Borée J, Foucher F. Experimental combustion analysis in a gasoline baseline hydrogen-fueled internal combustion engine at ultra-lean conditions. In: SAE technical papers. SAE International; 2023. https://doi.org/10.4271/2023-24-0073.
[31] Sfriso S et al. Proposal and validation of 3D-CFD framework for ultra-lean hydrogen combustion in ICEs; 2024. https://doi.org/10.4271/2024-01-2685.
[32] Cicalese G, Berni F, Fontanesi S. Integrated in-cylinder/CHT methodology for the simulation of the engine thermal field: an application to high performance turbocharged DISI engines. SAE Int J Engines 2016;9(1):601–17. https://doi.org/10.4271/2016-01-0578.
[33] Berni F, Cicalese G, Fontanesi S. A modified thermal wall function for the estimation of gas-to-wall heat fluxes in CFD in-cylinder simulations of high performance spark-ignition engines. Appl Therm Eng 2017;115:1045–62. https://doi.org/10.1016/j.applthermaleng.2017.01.055.
[34] Cicalese G, Berni F, Fontanesi S, D'Adamo A, Andreoli E. A comprehensive CFD-CHT methodology for the characterization of a diesel engine: from the heat transfer prediction to the thermal field evaluation. In: SAE technical papers. SAE International; 2017. https://doi.org/10.4271/2017-01-2196.
[35] Yakhot V, Orszag SA. Renormalization group analysis of turbulence. I. Basic theory. J Sci Comput 1986;1(1):3–51. https://doi.org/10.1007/BF01061452.
[36] Siemens Industries Digital Software. STAR-CD Methodology, version 2205.0001, Siemens 2022.
[37] Teodosio L, Berni F. Optimization via genetic algorithm of a variable-valve-actuation spark-ignition engine based on the integration between 1D/3D simulation codes and optimizer. Int J Engine Res 2022. https://doi.org/10.1177/14680874221099874.
[38] Berni F, et al. A zonal secondary break-up model for 3D-CFD simulations of GDI sprays. Fuel 2022;309. https://doi.org/10.1016/j.fuel.2021.122064.
[39] Iacovano C, Berni F, Barbato A, Fontanesi S. A preliminary 1D-3D analysis of the Darmstadt research engine under motored condition. In: E3S web of conferences. EDP Sciences; 2020. https://doi.org/10.1051/e3sconf/202019706006.
[40] Sparacino S, Berni F, Riccardi M, Cavicchi A, Postrioti L. 3D-CFD simulation of a GDI injector under standard and flashing conditions. In: E3S web of conferences. EDP Sciences; 2020. https://doi.org/10.1051/e3sconf/202019706002.
[41] Sparacino S, Berni F, D'Adamo A, Krastev VK, Cavicchi A, Postrioti L. Impact of the primary break-up strategy on the morphology of GDI sprays in 3D-CFD simulations of multi-hole injectors. Energies (Basel) 2019;12(15). https://doi.org/10.3390/en12152890.
[42] Berni F, et al. Modeling of gaseous emissions and soot in 3D-CFD in-cylinder simulations of spark-ignition engines: a methodology to correlate numerical results and experimental data. Int J Engine Res 2022. https://doi.org/10.1177/14680874221112564.
[43] Berni F, Cicalese G, Borghi M, Fontanesi S. Towards grid-independent 3D-CFD wall-function-based heat transfer models for complex industrial flows with focus on in-cylinder simulations. Appl Therm Eng 2021;190. https://doi.org/10.1016/j.applthermaleng.2021.116838.
[44] Berni F, Fontanesi S. A 3D-CFD methodology to investigate boundary layers and assess the applicability of wall functions in actual industrial problems: a focus on in-cylinder simulations. Appl Therm Eng 2020;174. https://doi.org/10.1016/j.applthermaleng.2020.115320.
[45] Berni F, Cicalese G, Sparacino S, Cantore G. On the existence of universal wall functions in in-cylinder simulations using a low-Reynolds RANS turbulence model. In: AIP Conference Proceedings. American Institute of Physics Inc.; 2019. https://doi.org/10.1063/1.5138752.
[46] d'Adamo A, Iacovano C, Fontanesi S. Large-Eddy simulation of lean and ultra-lean combustion using advanced ignition modelling in a transparent combustion chamber engine. Appl Energy 2020;280. https://doi.org/10.1016/j.apenergy.2020.115949.
[47] D'Adamo A, Breda S, Cantore G. Large-eddy simulation of cycle-resolved knock in a turbocharged SI engine. In: Energy Procedia. Elsevier Ltd; 2015. p. 45–50. https://doi.org/10.1016/j.egypro.2015.11.881.
[48] Herweg R, Maly RR. A fundamental model for flame kernel formation in SI engines. SAE Trans 1992;101:1947–76. http://www.jstor.org/stable/44611342.
[49] Herweg R, Maly RR. A fundamental model for flame kernel formation in SI engines. J Engines 1992. https://doi.org/10.4271/922243.
[50] Trelles JP, Heberlein JVR, Pfender E. Non-equilibrium modelling of arc plasma torches. J Phys D Appl Phys 2007;40(19):5937–52. https://doi.org/10.1088/0022-3727/40/19/024.
[51] Trelles JP, Chazelas C, Vardelle A, Heberlein JVR. Arc plasma torch modeling. J Therm Spray Technol 2009;18(5–6):728–52. https://doi.org/10.1007/s11666-009-9342-1.
[52] Haidar J. Non-equilibrium modelling of transferred arcs. J Phys D Appl Phys 1999;32:263–72.
[53] Gleizes A, Gonzalez JJ, Freton P. Thermal plasma modelling. J Phys D Appl Phys 2005;38(9). https://doi.org/10.1088/0022-3727/38/9/R01.
[54] Lucchini T, et al. A comprehensive model to predict the initial stage of combustion in SI engines. In: SAE technical papers. SAE International; 2013. https://doi.org/10.4271/2013-01-1087.
[55] Willems H, Sierens R. Modeling the initial growth of the plasma and flame kernel in SI engines. J Eng Gas Turbine Power 2003;125(2):479–84. https://doi.org/10.1115/1.1501912.
[56] Colin O, Benkenida A. The 3-zones extended coherent flame model (Ecfm3z) for computing premixed/diffusion combustion. Oil Gas Sci Technol 2004;59(6):593–609. https://doi.org/10.2516/ogst:2004043.
[57] SIEMENS PLM. DARS v2020.1 manual – book 2; 2020.
[58] Konnov AA. Refinement of the kinetic mechanism of hydrogen combustion. Adv Chem Phys 2004;23:5–18.
[59] SIEMENS PLM. STARCD v4.34 manual – methodology; 2020.
[60] Sfriso S, Berni F, Fontanesi S, D'Adamo A, Antonelli M, Frigo S. A 3D-CFD numerical approach for combustion simulations of spark ignition engines fuelled with hydrogen: a preliminary analysis; 2023. https://doi.org/10.4271/2023-01-0207.
[61] Matalon M. The Darrieus-Landau instability of premixed flames. Fluid Dyn Res 2018;50(5). https://doi.org/10.1088/1873-7005/aab510.
[62] Fogla N, Creta F, Matalon M. Effect of folds and pockets on the topology and propagation of premixed turbulent flames. Combust Flame 2015;162(7):2758–77. https://doi.org/10.1016/j.combustflame.2015.04.012.
[63] Al-Shahrany AS, Bradley D, Lawes M, Liu K, Woolley R. Darrieus–Landau and thermo-acoustic instabilities in closed vessel explosions. Combust Sci Technol 2006;178(10–11):1771–802. https://doi.org/10.1080/00102200600788734.
[64] Berger L, Attili A, Gauding M, Pitsch H. Effects of Karlovitz number variations on thermodiffusive instabilities in lean turbulent hydrogen jet flames. Proc Combust Inst 2024;40(1–4):105219. https://doi.org/10.1016/j.proci.2024.105219.
[65] Bradley D, Gaskell PH, Gu XJ, Sedaghat A. Premixed flamelet modelling: Factors influencing the turbulent heat release rate source term and the turbulent burning velocity. Combust Flame 2005;143(3):227–45. https://doi.org/10.1016/j.combustflame.2005.05.014.
[66] Bradley D, Lawes M, Liu K, Mansour MS. Measurements and correlations of turbulent burning velocities over wide ranges of fuels and elevated pressures. Proc Combust Inst 2013;34(1):1519–26. https://doi.org/10.1016/j.proci.2012.06.060.
[67] Bruneaux G. Asymptotic analysis, direct numerical simulation and modeling of premixed turbulent flame-wall interaction; Etude asymptotique, simulation numerique directe et modelisation de l'interaction flamme turbulente premelangee-paroi. Ph.D. Thesis. 92 – Rueil-Malmaison (France): Institut Francais du Petrole (IFP); 1996.
[68] Peters N. Turbulent combustion, vol. 12(11). Cambridge University Press; 2000. https://doi.org/10.1017/CBO9780511612701.
[69] Ramalho Leite C, Brequigny P, Borée J, Foucher F. Early flame development characterization of ultra-lean hydrogen–air flames in an optical spark-ignition engine. Proc Combust Inst 2024;40(1–4):105260. https://doi.org/10.1016/j.proci.2024.105260.
[70] Berger L, Attili A, Pitsch H. Synergistic interactions of thermodiffusive instabilities and turbulence in lean hydrogen flames. Combust Flame 2022;244:112254. https://doi.org/10.1016/j.combustflame.2022.112254.
[71] Chu H, Berger L, Gauding M, Pieper S, Pitsch H. Interactions of preferential diffusion and mixture inhomogeneities in hydrogen and iso-octane flame kernels under engine conditions. Combust Flame 2025;274:113991. https://doi.org/10.1016/j.combustflame.2025.113991.